The resting and ligand-bound states of the membrane-embedded human T-cell receptor–CD3 complex

Ryan Q. Notti[1,2,*], Fei Yi[3,4], Søren Heissel[5], Martin W. Bush[1], Zaki Molvi[6], Pujita Das[1], Henrik Molina[5], Christopher A. Klebanoff[2,3,4], and Thomas Walz[1]

[1] Laboratory of Molecular Electron Microscopy, The Rockefeller University, New York, NY

[2] Department of Medicine, Memorial Sloan Kettering Cancer Center, New York, NY

[3] Human Oncology Pathogenesis Program, Memorial Sloan Kettering Cancer Center, New York, NY

[4] Parker Institute for Cancer Immunotherapy, Memorial Sloan Kettering Cancer Center, New York, NY

[5] Proteomics Resource Center, The Rockefeller University, New York, NY

[6] Immunology Program, Memorial Sloan Kettering Cancer Center, New York, NY

* To whom correspondence should be addressed: rnotti@rockefeller.edu

Summary

The T-cell receptor (TCR) is central to the ligand-dependent activation of T lymphocytes and as such orchestrates both adaptive and pathologic immune processes[1]. However, major questions remain regarding the structure and function of the human TCR[2–4]. Here, we present cryogenic electron microscopy structures for the unliganded and HLA-bound human TCR–CD3 complex in nanodiscs that provide a native-like lipid environment. The unliganded structures reveal two related conformations that are distinct from its structure in detergent. These new “closed and compacted” conformations afford insights into the interactions between the TCR–CD3 and the membrane, including conserved surface patches that make extensive outer leaflet contact, and suggest novel conformational regulation by glycans. We show that the closed/compacted

26 conformations, not the extended one previously reported in detergent[5–8], represent the
27 unliganded resting state for the TCR–CD3 *in vivo*, underscoring the importance of structural
28 interrogation of membrane proteins in native-like environments. By contrast, the structure of the
29 HLA-bound complex in nanodiscs is in an open and extended conformation, showing that
30 physiologic ligand binding is sufficient to induce substantial conformational change in the TCR–
31 CD3 complex. We use conformation-locking disulfide mutants to show that ectodomain opening
32 is necessary for maximal ligand-dependent TCR–CD3 activation, demonstrating that TCR-
33 intrinsic conformational change is necessary for full TCR–CD3 activation and opening numerous
34 avenues for immunoreceptor engineering.
35
36 **Main**
37 T cells are central to a wide array of both adaptive and pathologic immune responses. The T-
38 cell receptor (TCR), in association with members of the CD3 protein family, allows T cells to
39 recognize and respond to antigenic peptides presented on human leukocyte antigen (HLA)
40 complexes of other cells. While the identities of the TCR–CD3 complex constituents and its
41 downstream signaling elements have been known for some time, questions remain regarding its
42 activation mechanism.
43 The TCR–CD3 is a hetero-octameric membrane protein complex[5–8]. The αβ-type TCR is
44 comprised in part by two variable chains, TCRα and TCRβ, which directly interface with the
45 HLA–antigen complex. Antigen specificity is generated through somatic recombination of the
46 variable segments in the TCRα and TCRβ genes. The remainder of the core complex is
47 comprised of six invariant CD3 family chains: the CD3γ-CD3ε and CD3δ-CD3ε heterodimers,
48 and a CD3ζ homodimer. Herein, we differentiate the CD3ε protomers by the CD3 component

with which each pairs (CD3ε_D pairs with CD3δ, and CD3ε_G pairs with CD3γ) and the CD3ζ protomers as CD3ζ and CD3ζ'.

While the TCRα and TCRβ chains lack intracellular signaling domains, the CD3 proteins possess cytoplasmic immunoreceptor tyrosine activation motifs (ITAMs) that become phosphorylated upon TCR-HLA interaction and then bind and activate downstream signaling kinases. Dynamic interactions between ITAMs and the membrane regulate signaling[9,10], but the mechanism by which ligand binding to the extracellular TCRα-TCRβ domains results in phosphorylation of cytoplasmic CD3 ITAMs remains a matter of debate. Specifically, it is unclear whether ligand binding and activation involves conformational change in the TCR–CD3 complex. While reconstitution of TCR–CD3 signaling *in vivo* with minimal constructs has argued against transmembrane conformational change[11], biochemical evidence in support of conformational change[12–15] and specifically for reversible structural extension of the TCR under mechanical force suggests the opposite[16], although the structural details of such conformational transitions remain to be determined.

Structures of the hetero-octameric $\alpha\beta$-type TCR–CD3 have been determined by cryogenic electron microscopy (cryo-EM)[5–8]. These studies revealed an antenna-like structure, with the TCRα and TCRβ variable domains projecting over a ring formed by the CD3 ectodomains and the TCRα and TCRβ constant domains, with numerous interactions between their respective transmembrane (TM) helices (Extended Data Figure 1a). Addition of HLA-antigen to this complex did not meaningfully alter the conformation of the TCR–CD3[7,8], arguing against models of intrinsic conformational change in the ligand-dependent TCR–CD3 activation process (Extended Data Figure 1a,b).

However, the TCR–CD3 complexes used in these studies were solubilized in detergent. Biochemical data have previously shown important roles for the lipid bilayer in the regulation of

73 TCR–CD3 signaling specifically[6,17,18], raising questions as to the physiologic relevance of the
74 determined structures. Membrane protein structure determination is generally preferable in a
75 native-like membrane environment that increases the likelihood that important protein–lipid
76 interactions are captured in the obtained molecular models[19].

77 Here, we report cryo-EM structures of a human TCR–CD3 stabilized both in detergent
78 micelles and nanodiscs. The structures reveal novel conformations for the TCR–CD3 in a
79 native-like lipid environment, distinct from those previously reported, and cross-linking data
80 support the notion that these conformations represent the resting state of an unstimulated TCR–
81 CD3 on T cells. We then determined the structure of the same nanodisc-embedded TCR–CD3
82 complex bound to HLA, revealing substantial conformational change upon physiologic ligand
83 binding, and show that exit from the resting state conformation is required for maximal TCR–
84 CD3 signaling.

85

86 **Results**

87 *Structure of the NY-ESO-1-specific 1G4 TCR–CD3 in detergent micelles.* In this study, we
88 investigated the structure of the 1G4 (LY-variant) TCR–CD3. We chose the 1G4 TCR, which
89 binds to an HLA-A*02:01-restricted 9 amino acid epitope derived from the NY-ESO-1 cancer-
90 testis antigen, because it is both a model immunoreceptor and being developed as an anti-
91 cancer therapeutic[20]. To confirm that 1G4 has a similar structure to the other TCR–CD3
92 complexes analyzed in detergent, we purified this complex in glyco-diosgenin (GDN) and
93 determined its structure by cryo-EM to a nominal resolution of 3.3 Å (Figure 1a; Extended Data
94 Figure 1c-f; Extended Data Table 1; Supplementary Methods Figures 1, 2, 6, 7; Supplementary
95 Methods Tables 4, 7). Herein, this model and the conformation it represents will be abbreviated
96 as “GDN.” Overall, GDN was very similar to the structures of three other TCR–CD3 constructs,
97 including those with and without HLA bound (Extended Data Figure 1g). This is not surprising,

98 given the nearly identical CD3 and TCR constant region sequences shared by these receptors
99 (Extended Data Figure 1h).
100
101 *Structure of the TCR–CD3 in a native-like lipid environment.* To determine the structure of the
102 1G4 TCR–CD3 in a native-like lipid environment, we reconstituted the TCR–CD3 complex into
103 membrane scaffold protein-based nanodiscs loaded with mammalian polar lipids and cholesteryl
104 hemisuccinate (Supplementary Methods Figure 1). Computational processing of cryo-EM data
105 yielded two distinct maps determined to nominal resolutions of 3.3 to 3.1 Å (for locally refined
106 maps used for model building and refinement; Extended Data Figure 2; Supplementary Methods
107 Figures 3, 4, 6; Supplementary Methods Table 5). These maps, which we denote as nanodisc
108 (ND)-I and ND-II, were clearly different from GDN (Figure 1) and the previously published TCR
109 structures. Attempts to bias the particle search towards the published conformations with
110 projections of the structure in detergent or that same structure docked into a lipid nanodisc
111 model did not yield any maps approximating the previously published conformation
112 (Supplementary Methods Figure 3).
113 Despite equal or higher nominal overall resolutions than GDN, ND-I and ND-II were not
114 as high quality (compare local resolution estimations in Extended Data Figure 2d,h with
115 Extended Data Figure 1f). This was likely due to a high degree of conformational variability, but
116 also due in part to map anisotropy (compare Extended Data Figure 2c,g to Extended Data
117 Figure 1e). Efforts to improve the orientation distribution of the particles with graphene oxide
118 grids and/or fluorinated detergents did not improve reconstruction quality. Nonetheless, these
119 maps were of sufficient quality to build models into the density, with much of the density having
120 estimated local resolution of better than 4 Å.
121 Molecular models were built for ND-I and ND-II by docking the GDN structure into the
122 maps and refining them by standard approaches (Extended Data Table 1; Supplementary

123 Methods Figures 6, 7; Supplementary Methods Table 7; see Supplementary Methods for
124 details). These models reveal two distinct but related conformations of the TCR–CD3 complex
125 (Figure 1a). The ND structures show two large conformational changes relative to GDN: a
126 "closure" of the TCR ectodomains against the CD3 ectodomains (Figure 1a,b) and a
127 "compaction" of the juxtamembrane (JM) linker peptides (Figure 1a,c,d). Collectively, these
128 changes shorten the TCR projection into the extracellular milieu by approximately 35 Å. Closure
129 of the TCR ectodomains (Figure 1b) results in part from rotation of the variable domains towards
130 their respective constant domains about the interdomain hinge region (Extended Data Figure
131 3a,b). Relative to the "extended" JM linker conformations seen in GDN, the CD3 JM linkers are
132 compacted, with closer approximation of the CD3 ectodomains to the amino-terminal ends of
133 their TM helices (Figure 1c,d).

134 The conformational changes in the TCR ectodomains are accompanied by rotations of
135 TM helices. While the in-plane arrangement of the TM helices is largely similar when viewed
136 along the membrane normal (Figure 1e), examination from orthogonal axes reveals differences
137 in TM helix conformation. Compaction of the CD3 JM linkers requires opening of the angle
138 between the TM helices of the CD3$\varepsilon\delta$ and CD3$\varepsilon\gamma$ pairs by 23° (from 31° to 54°) and 28° (from
139 39° to 67°), respectively, when comparing ND-II with GDN (Figure 1c,d). For ND-I, the TM
140 helices of the CD3$\varepsilon\delta$ are bent, with the first helical turn displaying a wide splay (76°, Extended
141 Data Figure 3c), but the overall angle between the modeled helices (46°) is intermediate to ND-
142 II and GDN. The CD3ε_G TM helix was not modeled, as its register could not be confirmed, and
143 thus the CD3$\varepsilon\gamma$ TM angle was not measured. Additionally, there is splaying of the TCRβ and
144 distal CD3ζ TM helices away from the membrane normal (Figure 1f). In GDN, the TCRα TM
145 helix extends outward past the amino-terminal ends of the CD3 TM helices, where it is
146 ensconced by the extended CD3 JM linkers. Compaction of the JM linkers in nanodiscs

147 necessitates reorganization of the first turn of the TCRα TM helix, which is unstructured and
148 displaced towards the lipid bilayer (Figure 1f). Taken together, these cryo-EM maps reveal
149 marked conformational differences between the TCR–CD3 in detergent micelles and a lipid
150 bilayer.

151 Additionally, the transmembrane helices of ND-I and ND-II appear shorter than in GDN.
152 Specifically, these structures lack clear density for the cluster of basic and aromatic amino acids
153 visualized in GDN that extend the TM helices (Extended Data Figure 3d). In a membrane, these
154 extensions would likely be interfacial or extend into the cytoplasm[21]. Although there is additional
155 density beyond the modeled carboxy-termini of some of these shortened helices in ND-I and
156 ND-II, it is not of sufficient quality to model with confidence (Extended Data Figure 3e,f). This
157 suggests the TCR–CD3 TM helices are less rigid in the inner leaflet of a lipid bilayer than in a
158 detergent micelle.

159

160 *Lipid interactions with the TCR–CD3.* The TCR–CD3 is known to interface directly with
161 membrane cholesterol[22], and the binding sites have been visualized in previously published
162 structures[6]. In GDN, ND-I, and ND-II, density corresponding to two cholesterols in the previously
163 published structures was again apparent (Extended Data Figure 3g). The two cholesterol
164 molecules in ND-I and ND-II are oriented tail-to-tail in a groove between CD3ζ', TCRα, TCRβ,
165 and CD3γ, as in GDN (Figure 2a). However, the compaction-associated changes in the TCR–
166 CD3 TM helices result in a sliding of the cholesterol molecules towards each other, with
167 deflection of their branched aliphatic tails to prevent clashing (Figure 2a, insets). We refer to the
168 cholesterol molecules as $Chol_A$ and $Chol_B$, corresponding to the TCR–CD3 TM helix with which
169 each is approximated. The deflected tail of $Chol_B$ is interposed between adjacent TM helices,
170 accommodated by their increased splay in the compact conformation (Figure 2b, inset). The

171 cholesterol-binding groove is more open to the membrane bilayer in nanodiscs, creating a
172 possible path for cholesterol loading into the assembled TCR–CD3 and/or exchange with the
173 membrane environment (Figure 2b, bottom left).

174 Imaging of the TCR–CD3 in a lipid bilayer revealed additional sites of protein–lipid
175 interaction. Unmodeled tubular densities consistent with phospholipid acyl chains are present at
176 several sites adjacent to the TCR–CD3 TM helices (yellow densities in Extended Data Figure
177 3h-k). Structured lipid is seen parallel to the tail-to-tail cholesterol dimer, filling the
178 aforementioned channel between the cholesterol-binding groove and the bulk membrane lipids
179 (red dashed circle in Figure 2b, bottom left; Extended Data Figure 3h). Splay of the CD3ζ TM
180 helix away from that of CD3ε_D enlarges a cavity, which is filled by several presumptive lipid acyl
181 chains in the nanodisc (Extended Data Figure 3k). Additional probable sites of structured lipid
182 include a shroud of density over the CD3ζ TM helices (Extended Data Figure 3i) and in the cleft
183 over the TCR$\alpha\beta$ TM helices between CD3δ and CD3ε_G (Extended Data Figure 3j).

184 The ND-I and ND-II maps show clear density for the proteolipid nanodisc that enshrouds
185 not only the TM helices, but also the membrane-proximal faces of the TCR–CD3 ectodomains
186 (Figure 3a, left). The lipid contacts with the CD3 ectodomains are apparent even in maps
187 contoured at a higher threshold, consistent with high occupancy (Figure 3a, right). While the
188 CD3 ectodomain surfaces are generally poorly evolutionarily conserved in comparison to the
189 TM helices, patches on the membrane-proximal surfaces of the CD3 ectodomains do show high
190 sequence conservation (Figure 3a,c). These highly conserved ectodomain surface patches
191 (black triangles in Figure 3b-e) interface with the extracellular membrane leaflet and are neutral
192 to electropositive (Figure 3e), facilitating phospholipid head group interactions. Of note, we
193 observe a similar conserved electropositive patch at the interface of CD79$\alpha\beta$[23], the analogous
194 ITAM-bearing chains in the B-cell receptor, raising the prospect that this interface may also

195 favor membrane interactions and a different conformation in the lipid bilayer from that reported
196 in detergent micelles (Extended Data Figure 4).
197
198 *Probing TCR conformation in situ*. Which conformation of the TCR–CD3 is the physiologic
199 resting state on the cell membrane: the open/extended conformation seen in detergent micelles,
200 or the closed/compacted conformations seen in the lipid bilayer of the nanodisc? Given that the
201 lipid bilayer of a nanodisc more closely approximates the physicochemical milieu of the plasma
202 membrane, we hypothesized that the TCR–CD3 is closed and compacted in the absence of
203 activating ligand *in vivo.* To test this notion, we engineered a series of disulfide bonds that would
204 only be geometrically favorable in ND-I and/or ND-II but not GDN (or *vice versa*), and we read
205 out their presence or absence by one of the following approaches: (1) non-reducing sodium
206 dodecyl sulfate-polyacrylamide gel electrophoresis (SDS-PAGE) and Western blot of whole-cell
207 lysates for interchain disulfides, or (2) mass spectrometry on affinity-purified protein for
208 intrachain disulfides. Analysis of disulfide bonds in the Protein Databank have shown that
209 disulfide bonds almost never have a Cys-Cys Cα-Cα distance greater than 7 Å, with most being
210 between 5 and 6.5 Å[24]. Accordingly, we sought residue pairs in the TCR–CD3 ectodomains with
211 Cα-Cα distances below 7 Å in one conformation and above 7 Å in the other as candidates for
212 disulfide engineering.
213 The interface between CD3δ and TCRα contains several pairs of residues with geometry
214 favorable for engineered disulfide formation in ND-I but not GDN (Figure 4a). As TCRα and
215 TCRβ are linked by an interchain disulfide natively (Extended Data Figure 5a), formation of a
216 TCRα–CD3δ disulfide would result in an upward gel shift of the TCRαβ heterodimer in
217 nonreducing SDS-PAGE. For all three tested engineered disulfide pairs meeting the 7 Å Cα-Cα
218 distance constraint, a gel shift consistent with TCRα–CD3δ disulfide formation was observed

219 (Figure 4b, asterisks; all full-length gels in Supplementary Methods Figure 9). Confirming that
220 this mass shift was due to disulfide formation, no gel shift was apparent under reducing
221 conditions (Supplementary Methods Figure 9b). Moreover, the mass shift was due to the
222 formation of the engineered disulfide and not an off-target bond, as adduct formation was only
223 seen when both residues in a given target pair were mutated to cysteines (Figure 4b). As an
224 internal negative control, a permutation of cysteine mutants at this interface not meeting
225 geometric criteria for disulfide formation in ND-I (TCRα S78C – CD3δ N38C, Figure 4a, right,
226 orange labels) was produced. It did not form a disulfide *in vivo* (Figure 4b, orange) despite S78C
227 and N38C successfully pairing with cognate cysteine mutants that did meet the inter-Cα
228 threshold. This control shows the structural precision and specificity of the engineered disulfide
229 bond approach. These experiments were performed using whole-cell lysates, but we obtained
230 similar results with NiNTA affinity-purified protein (Extended Data Figure 5b), and we were able
231 to reconstitute the two G79C-crosslinked mutants into nanodiscs (Extended Data Figure 5c,d),
232 suggesting proper folding and assembly of the holo TCR–CD3.

233 The region around the TCRα and TCRβ interdomain hinges is also notably different in
234 the closed/compacted conformation compared to the open/extended one, with the variable
235 domains coming into closer apposition with their respective constant domains, allowing the
236 engineering of conformation-specific disulfide pairs in this region (Figure 4c,d). We probed
237 formation of these intrachain disulfides by mass spectrometry. Proteolytic digestion of the TCR–
238 CD3 with trypsin and chymotrypsin yielded distinct peptides, several of which were linked by
239 disulfide-bonds. Electron-transfer/higher-energy collision dissociation (EThcD) fragmentation
240 was used to fragment the disulfide-bonded peptides providing *in vacuo* reduction to the linear
241 peptide constituents along with peptide backbone fragmentation, thereby allowing unambiguous
242 identification of the engineered disulfides[25]. All native TCR–CD3 disulfides spanning two

243 proteolytic fragments (Extended Data Figure 5a) were observed in the wild-type 1G4 TCR–CD3
244 by this approach (Extended Data Table 2). For both ND conformation-compatible engineered
245 disulfides tested (Figure 4c,d), we observed formation of the engineered disulfide (Figure 4e,f;
246 Extended Data Table 2). In contrast, an engineered disulfide that would only be present in the
247 open/extended conformation (Extended Data Figure 5e) did not form *in vivo* (Extended Data
248 Table 2). Taken together, these data support the conclusion that a TCR–CD3 in the unliganded,
249 resting state adopts the closed/compact conformation *in vivo*.
250
251 *Conformational variability of the TCR–CD3 in a lipid bilayer*. To allow direct comparison of the
252 two distinct, but related, closed/compacted structures (ND-I and ND-II), they were aligned by
253 their TCRα TM helices. TCRα was chosen because it is relatively perpendicular to the
254 membrane plane (alongside CD3ζ') and thus might be least affected by any differences in TM
255 helix splay. Indeed, this alignment strategy brought the nanodisc density of their maps into
256 alignment as well (Extended Data Figure 6a), giving both models the same orientation relative
257 to the membrane bilayer. In contrast to the strong overall alignment of the TCR–CD3 TM helices
258 by this approach (Extended Data Figure 6b,c), the ectodomains of ND-I and ND-II have marked
259 conformational differences, as seen in the aligned cryo-EM densities (Extended Data Figure
260 6a,b) and the resulting protein models (Figure 5a). Comparison of the structures reveals the
261 motions allowing exchange between these conformations (Figure 5b,c; Supplementary Movie
262 1). ND-I is the most closed of the three structures, and transition to ND-II requires several
263 motions: the depression of the CD3ε_D (Figure 5b) and CD3γ ectodomains (Figure 5c) away from
264 the TCR variable domains and towards the bilayer outer leaflet; rotation of the of the TCRα
265 variable domain about the interdomain hinge (Figure 5b); and retraction of the TCRβ variable
266 domain (Figure 5c). This is accompanied by sliding of CD3ζ along its helical axis towards the

267 ectodomains (Figure 5b). While the TCRα and CD3ζ' TM helices remain relatively fixed in this
268 frame of reference, the TCRβ and CD3γ TM helices shift away from the cholesterol-binding
269 groove (Figure 5d; Extended Data Figure 6c). To accommodate this movement, there is rotation
270 of $Chol_A$ and elevation of $Chol_B$ (Figure 5d), showing cholesterol to be an integral and dynamic
271 component of the TCR–CD3 structure.

272 The GDN map displays densities for many of the known asparagine (N)-linked glycans in
273 the TCR–CD3 (Extended Data Figure 6d). There were fewer densities modellable as N-linked
274 glycans in the ND-I and ND-II maps (Extended Data Figure 6d). However, all three maps show
275 an array of densities lateral to the CD3δ and TCRα ectodomains, corresponding to sites of
276 known N-linked glycosylation. In ND-II, the TCRα (linkage unclear) and CD3δ N74-linked
277 glycans are visible, emerging radially from the TCR–CD3, as in GDN, but are not well structured
278 (Figure 5e). By comparison, ND-I reveals clear reorganization of the glycans (Figure 5e), with
279 increased stacking of adjacent glycans brought into close proximity by tight ectodomain closure.
280 This arraying of N-linked glycans is reminiscent of that seen on HIV Env, where interacting
281 adjacent glycans form a structured arcade of glycan cores (Extended Data Figure 6e). Two
282 densities in the array are attributable to CD3δ N74- and TCRα N82-linked glycans, with a third
283 density emerging between them without definitive attribution (purple question mark in Figure 5e,
284 right inset). In GDN, as in other structures of TCR–CD3 in detergent, the CD3δ N38-linked
285 glycan is oriented inward towards the cleft between the TCR and CD3 ectodomains (Figure 5f,
286 top). In ND-II, CD3δ N38 is unstructured (Figure 5f, middle), but is grossly positioned at the
287 entrance to the cleft, and the linked glycan could conceivably orient either into or away from the
288 cleft. In ND-I, CD3δ N38 is structured (Figure 5f, bottom), but its glycan cannot be confidently
289 modeled. However, density protrudes from N38 into the open cleft (Figure 5f, asterisk) and

290 additional unmodeled density is seen within the cleft, consistent with the glycan remaining within
291 the cleft in the ND-I conformation.

292 The differences in ectodomain closure seen between ND-I and ND-II could have
293 consequences for the accessibility of the TCR variable domains to HLA-antigen complexes. To
294 assess the impact of ectodomain cleft opening and closure on TCR–HLA interactions, we
295 modeled the binding geometry of HLA onto GDN, ND-I, and ND-II by alignment of the TCR-HLA
296 crystal structure to the TCR variable domains in our models (Figure 5g). There appears to be
297 adequate clearance for the TCR variable domains to interact with HLA in GDN and ND-II. For
298 ND-I, the modeled fit is tighter, with the CD3ε_D ectodomain predicted to be in close contact with
299 HLA. However, on assessment of space-filling model cross-sections, no overt steric clashes are
300 evident (Figure 5h). Because a portion of a potentially clashing surface loop in the CD3ε_D
301 ectodomain is not modeled in ND-I, the TCR-aligned HLA model was docked into the ND-I cryo-
302 EM density (Figure 5i), but no unmodeled density appears to clash with HLA. The CD3ε_D
303 ectodomain from GDN is completely modeled and aligns closely with that from ND-I (Extended
304 Data Figure 6f, inset). As an additional sensitivity analysis, the GDN CD3ε_D ectodomain was
305 modeled into ND-I and the HLA interaction again assessed. While there is a small overlap in
306 their space-filling models (Extended Data Figure 6f), no large clashes are observed. Thus, while
307 it remains unclear what quantitative effect ectodomain cleft closure might have on HLA affinity,
308 particularly in the physiologic context of a glycosylated HLA molecule, it is at least plausible that
309 both ND-I and ND-II may be receptive to HLA binding.

310 While our modeling data suggest that HLA can bind to TCR–CD3 in the closed,
311 compacted resting state conformations, TCR–CD3 opening and/or extension may be necessary
312 for coreceptor interaction with HLA bound to the TCR–CD3. Modeling the HLA class II–CD4
313 complex onto GDN, ND-I, and ND-II reveals an unfavorable geometry for CD4 interaction with a

314 class II HLA when bound to a TCR–CD3 in the ND-I or ND-II conformation because of the
315 proximity of the TCR variable regions to the membrane (Extended Data Figure 6g), at least for
316 the CD4 conformation reported in the CD4-HLA-TCR ectodomains ternary complex crystal
317 structure[26]. In contrast, CD4–HLA can be accommodated in the open, extended GDN
318 conformation (Extended Data Figure 6g). The full ectodomain structure of the CD8 coreceptor
319 has not been described, precluding a similar analysis applicable to TCRs recognizing HLA class
320 I-restricted epitopes, like the one used in this study.
321
322 *TCR–CD3 conformational change upon HLA binding.* Whether or not the TCR–CD3 complex
323 undergoes conformational change upon binding to HLA remains an open question. To
324 determine the structure of the HLA-liganded TCR–CD3 complex in a lipid bilayer, we
325 reconstituted TCR–CD3 in nanodiscs as above, incubated the complex with an excess of single-
326 chain trimeric HLA–β2M–NY-ESO-1(C9V) (herein, "HLA"), and determined the structure by
327 single-particle cryo-EM (Extended Data Figure 7a,b,c; Extended Data Table 1; Supplementary
328 Methods Figures 5, 8; Supplementary Methods Tables 6, 7). Despite picking particles using a
329 template model of the closed, compacted TCR–CD3 complex bound to HLA, cryo-EM
330 reconstruction showed the HLA-bound complex to be in the open, extended conformation
331 (Figure 6a,b). Indeed, the HLA-bound conformation was nearly identical to that seen in GDN
332 (Figure 6c). There was subtle tilting of HLA relative to the TCR when comparing the HLA-bound
333 nanodisc structure to the crystal structure of the 1G4 TCRαβ ectodomain heterodimer bound to
334 HLA, but the binding interface was otherwise similar (Extended Data Figure 7d). Comparison of
335 the TCR variable domains in the HLA-bound nanodisc and GDN structures showed them to be
336 nearly identical, despite the absence of ligand in the GDN structure, and both were similar to the
337 crystal structure of the 1G4 TCRαβ ectodomain heterodimer bound to HLA (Extended Data

338 Figure 7e). By contrast, ligand binding induced a number of structural changes in the TCR
339 variable domains relative to ND-I and ND-II. Specifically, in ND-I and ND-II the amino-terminal
340 strands and several surface loops in the variable domains were unstructured, but these were
341 ordered in the HLA-bound structure (Supplementary Methods Table 7). Qualitatively, the HLA-
342 bound map showed better resolved protein density throughout (compare Figure 6a with Figure
343 1a), consistent with a general rigidification of the TCR structure upon HLA binding, as has been
344 observed previously for the TCR ectodomains by NMR[15] and hydrogen-deuterium exchange[27].
345 This rigidification was apparent in the density corresponding to the TCR variable domains,
346 particularly for TCRβ (Extended Data Figure 7f,g).

347 Structural comparison of the resting and HLA-bound TCR–CD3 in lipid bilayers
348 demonstrates that HLA binding is sufficient to induce substantial conformational changes in the
349 TCR–CD3 complex. Our data support a model in which the unliganded "resting" TCR–CD3
350 explores a thermally accessible spectrum of closed/compacted conformations from the most
351 closed ND-I to the more open ND-II, with HLA-binding triggering a change to the open/extended
352 conformation (Figure 6d). We favor this transition occurring via the ND-II conformation, which is
353 more open than ND-I and thus closer to the HLA-bound state along this trajectory. Morphing the
354 closed/compacted conformation to the open/extended one (Supplementary Movie 2) highlights
355 the straightening of the TM helices towards the membrane normal (that is, decreased splay,
356 Figure 6e). These changes in TM conformation add to the plausibility of the model, as they
357 provide a means to transmit conformational changes in the ectodomains to the cytoplasmic
358 ITAMs.

359 While some published data support pure allosteric activation models for the TCR, in
360 which HLA binding is sufficient to induce T-cell activation[28], other data support models in which
361 ligand-induced conformational change is necessary but not sufficient, requiring subsequent
362 receptor clustering[12] or mechanical force application[29]. However, all of these models propose

363 that TCR–CD3 conformational change is a necessary step in the activation process, and thus
364 we hypothesized that constraining conformational change would impair ligand-induced T-cell
365 activation. Transition from the closed/compacted to the open/extended conformations revealed
366 here requires further ectodomain opening from the ND-II state (Figure 6d). We hypothesized
367 that the intra-TCRα disulfide-forming double mutant S104C–V182C (characterized above,
368 Figure 4c) would prevent ectodomain opening to the HLA-bound conformation, as the Cα-Cα
369 distance between these residues in that conformation is outside the limits of a disulfide bond
370 (Figure 6f). To investigate the impact of restrained TCR–CD3 opening on ligand-dependent
371 activation of T cells, we introduced wild-type and TCRα S104C–V182C mutant TCR constructs
372 into TCRαβ-negative Jurkat T cells bearing an NFAT-responsive fluorescent reporter. TCR–
373 CD3 assembly and surface localization (as assessed by anti-CD3ε antibody binding) and HLA-
374 binding competence were confirmed by flow cytometry for the mutant and were comparable to
375 cells transduced with wild-type 1G4 (Figure 6g). In the absence of HLA-antigen tetramers, there
376 was no detectable reporter fluorescence in these cells, but upon exposure to HLA-antigen
377 tetramers, cells expressing wild-type TCR–CD3 became activated, with reporter fluorescence
378 peaking 16 h after HLA-tetramer addition (Figure 6h). By contrast, peak reporter fluorescence
379 was significantly decreased in the TCRα S104C–V182C mutant, with peak activation attenuated
380 by 26% relative to wild-type on exposure to 8 μg/mL of tetramers ($P < 0.05$, Figure 6d; source
381 data in Supplementary File 1). The TCRα S104C–V182C mutant and wild-type controls were
382 equally responsive to phorbol 12-myristate 13-acetate (PMA) and ionomycin, which bypass
383 TCR–CD3 signaling to activate T cells, showing this phenotype to be specific to ligand-induced
384 TCR–CD3 activation.
385
386 **Discussion**

387 Here, we report structures of a human TCR–CD3 both in a lipid bilayer and in detergent
388 micelles. We find that the TCR–CD3 hetero-octamer assumes a spectrum of more closed and
389 compacted conformations when embedded in a lipid bilayer relative to that seen in detergent
390 micelles, and that the closed/compacted conformation is indeed the native unliganded state of
391 the TCR–CD3. Addition of HLA, the physiologic ligand for the TCR, induced a change in
392 conformation from the resting state to an open/extended conformation like that previously seen
393 in detergent, and exit from the resting conformation by ectodomain opening is necessary for
394 maximal ligand-dependent activation of the TCR–CD3 complex. While this latter finding does
395 not rule out roles for TCR–CD3-extrinsic phenomena (e.g., higher-order clustering, steric
396 exclusion of inhibitory phosphatases) in the activation of the TCR–CD3 or regulation thereof, it
397 argues that intrinsic conformational change in the TCR–CD3 is necessary for early TCR–CD3
398 activation and argues against previous models that have excluded this requirement[11,30].
399 Similarly, it does not rule out a role for mechanical force application or catch bond formation in
400 the maximal activation of the TCR–CD3, but shows that the earliest stage of TCR activation
401 (i.e., conformational change out of the resting state) can be mediated by ligand binding alone.
402 Broadly, these findings reinforce the importance of structural interrogation of membrane
403 proteins in lipid environments that closely resemble their physiologic environment. Comparison
404 of TCR–CD3s in detergent micelles in the absence and presence of activating ligand had
405 revealed no change in TCR–CD3 structure[7,8], consistent with models excluding TCR–CD3
406 conformational change in the activation process. Although these studies were technically well
407 performed, our results now reveal that they did not identify the true resting state of the TCR–
408 CD3 complex in lipid bilayers, preventing observation of the conformational changes during
409 ligand-dependent activation.
410 Additionally, the structures in detergent did not capture the full scope of TCR–CD3
411 interaction with the membrane. Not only are membrane lipids closely interwoven with the TM

412 helices, but large conserved surface patches on the ectodomains mediate lipid–protein
413 interactions, likely partially counteracting the thermodynamic costs of JM linker compaction and
414 "spring loading" the TCR with potential energy for conformational change during activation. In
415 this model, ligand binding provides the activation energy to release the membrane-binding
416 surfaces of the CD3 ectodomains and allow JM extension. Detergent extraction would
417 overcome this thermodynamic barrier by removing the lipid bilayer all together. During
418 reconstitution into nanodiscs, we first extracted the TCR–CD3 complex in detergent, opening
419 and extending the receptor, which suggests that the addition of a lipid bilayer is sufficient to
420 reset the TCR–CD3 to its resting conformation without the need for extrinsic chaperones. Lastly,
421 we note that a similar conserved surface patch is present on the CD79 heterodimer in the B-cell
422 receptor[23], raising the possibility that other hetero-multimeric ITAM-containing immunoreceptors
423 exploit protein surface interactions with the lipid bilayer to constrain conformation.

424 As with the TCR–CD3 structures in detergent, the CD3 ITAMs are not visible in our
425 structures. The ITAMs are membrane-associated in the unliganded state[9,10], but are likely to be
426 radially disordered along the intracellular membrane face. However, the TM helix movements
427 seen between our closed/compacted and the open/extended conformations suggest a means
428 for communication of extracellular conformational changes in the TCR–CD3 complex to the
429 ITAMs. Within the cytoplasmic domains of CD3 proteins, the basic residues proximal to the CD3
430 TM helix are critical for ITAM association with the membrane[9,10]. Upon transition from the
431 receptive to the HLA-bound conformation, the decreased splay in the CD3 TM helices could
432 alter basic patch interaction with the membrane and favor ITAM release.

433 Analysis of the basal conformational heterogeneity of the TCR–CD3 suggests novel
434 means of TCR–CD3 regulation. The TCRα and CD3δ glycan ordering observed in the ND-I
435 conformation is notably different from the glycan arrangement in the more open ND-II
436 conformation or the TCR–CD3 in detergent. While molecular modeling of the branched glycan

437 sugars was not possible with sufficient confidence, the stacked arrangement of glycan core
438 densities raises the possibility of extensive hydrogen bonding between the glycan branches
439 distally and perhaps also with TCR–CD3 surface residues. While glycan–glycan and glycan–
440 protein interactions are well described *in trans*, there are fewer examples of structured glycan–
441 glycan interactions within a given protein or stable complex. The human immunodeficiency
442 virus-1 Env protein is an example of the latter[32,33] and the arrangement of the radial glycan array
443 in ND-I is reminiscent of that seen in crystallographic studies of Env. However, the stacking of
444 glycans observed in the TCR–CD3 is unique in being protein conformation-dependent. Breaking
445 an extensive glycan hydrogen-bonding network to transition out of ND-I would be energetically
446 costly, and thus modification of TCR–CD3 glycosylation could serve as a means of
447 posttranslational regulation of the TCR–CD3 activation threshold by increasing or decreasing
448 the free energy barrier to ND-I exit.

449 Previous studies have explored the role of cholesterol in the regulation of TCR–CD3
450 activation[6,18,22]. The substantive movements of the two cholesterol molecules seen between
451 TCR–CD3 conformations raise the possibility that changes in the sterol composition of the T-cell
452 membrane (either global or local) could alter TCR–CD3 activity even prior to ligand binding by
453 shaping the basal TCR–CD3 conformational landscape. Moreover, our structures reveal
454 channels for cholesterol loading or exchange with the lipid bilayer not previously observed,
455 making it plausible that already assembled TCR–CD3 could respond to changes in membrane
456 sterol content. Non-sterol lipid species are also known regulators of T-cell signaling[17], including
457 phosphoinositol lipids[34,35] and oxidized lipids in the tumor microenvironment[36]. This work
458 delineates multiple sites of structured interaction between the TCR–CD3 and membrane lipids
459 beyond the sterol-binding site, which may allow specific lipids to modulate TCR–CD3
460 conformation and activity.

The extensive contacts between TCR variable domain residues and those of the TCR constant domains or CD3 ectodomains in the closed/compacted conformations raises questions about how variation at these sites might confer specific baseline sensitivities to given TCR alleles. Whether use of certain V or J alleles changes the occupancy of different segments of the TCR–CD3 conformational landscape will need to be determined and has broad implications for vaccine design and immunotherapy engineering. Likewise, whether individually rare germline coding variants in the TCR constant domain *loci* or CD3 proteins affect an individual's basal T-cell reactivity is unclear outside of known deleterious loss-of-function alleles[37]. Such information might predict individual propensity for autoimmunity or responsiveness to immune-oncology agents and will provide insights for engineering TCRs with favorable activity profiles[38].

Methods

Full methods are detailed in the Supplementary Methods.

Data Availability Statement

Cryo-EM maps and atomic coordinates for GDN, ND-I, ND-II, and HLA-bound have been deposited in the Protein Data Bank and Electron Microscopy Data Bank with the following accession numbers: GDN, PDB 9BBC, EMD-44417; ND-I, PDB 8TW4, EMD-41658; ND-II, PDB 8TW6, EMD-41660; HLA-bound, PDB 9C3E, EMD-45166.

Acknowledgements

The authors thank the members of the Walz, T. de Lange (RU), and R. K. Hite (MSKCC) labs and Drs. E. L. Reinherz (HMS, DFCI) and W. D. Tap (MSKCC) for insightful conversations. We thank M. Ebrahim, J. Sotiris, and H. Ng at the Evelyn Gruss Lipper Cryo-EM Resource Center of The Rockefeller University for assistance with cryo-EM data collection. R.Q.N. was supported

486 by National Institutes of Health (NIH) grants T32CA9207, KL2TR001865, and UL1TR001866;
487 the Black Family Metastasis Center at Rockefeller University; and the Shapiro-Silverberg Fund
488 for the Advancement of Translational Research. This work was also supported by the Mark
489 Foundation for Cancer Research (R.Q.N. and T.W.). C.A.K. was supported, in part, by NIH
490 grants R37 CA259177, R01 CA269733, R01 CA286507, P30 CA008748, and P50 CA217694;
491 Cycle for Survival and the Shteinbuk and Mead Family; the Metropoulos Family Foundation; the
492 Parker Institute for Cancer Immunotherapy; and The Sarcoma Center at MSKCC. Mass
493 spectrometry data were generated by the Proteomics Resource Center at The Rockefeller
494 University (RRID:SCR_017797) using instrumentation funded by the Sohn Conferences
495 Foundation and the Leona M. and Harry B. Helmsley Charitable Trust.
496

497 **Author Contributions**

498 R.Q.N. conceived of the project, designed and performed experiments, analyzed data, built
499 models, and wrote and revised the manuscript; F.Y. designed and performed experiments and
500 analyzed data; S.H. designed and performed experiments and analyzed data; M.B. performed
501 experiments and analyzed data; H.M. designed and performed experiments and analyzed data;
502 Z.M. designed and performed experiments, P.K.D. performed experiments, C.A.K. designed
503 experiments, analyzed data, and revised the manuscript; T.W. designed experiments, analyzed
504 data, and revised the manuscript.
505

506 **Competing Interests**

507 C.A.K. is an inventor on patents related to TCR discovery and public neoantigen-specific TCRs
508 and is recipient of licensing revenue shared according to MSKCC institutional policies. C.A.K.
509 has consulted for or is on the scientific advisory boards for Achilles Therapeutics, Affini-T
510 Therapeutics, Aleta BioTherapeutics, Bellicum Pharmaceuticals, Bristol Myers Squibb,

Catamaran Bio, Cell Design Labs, Decheng Capital, G1 Therapeutics, Klus Pharma, Obsidian Therapeutics, PACT Pharma, Roche/Genentech, Royalty Pharma, and T-knife. C.A.K. is a scientific co-founder and equity holder in Affini-T Therapeutics.

References

1. Janeway, C. A. *et al. Immunobiology*. (Garland Science, 2001).
2. Reinherz, E. L. The structure of a T-cell mechanosensor. *Nature* **573**, 502–504 (2019).
3. Courtney, A. H., Lo, W.-L. & Weiss, A. TCR Signaling: Mechanisms of Initiation and Propagation. *Trends Biochem. Sci.* **43**, 108–123 (2018).
4. Mariuzza, R. A., Agnihotri, P. & Orban, J. The structural basis of T-cell receptor (TCR) activation: An enduring enigma. *J. Biol. Chem.* **295**, 914–925 (2020).
5. Dong, D. *et al.* Structural basis of assembly of the human T cell receptor–CD3 complex. *Nature* **573**, 546–552 (2019).
6. Chen, Y. *et al.* Cholesterol inhibits TCR signaling by directly restricting TCR-CD3 core tunnel motility. *Mol. Cell* **82**, 1278-1287.e5 (2022).
7. Sušac, L. *et al.* Structure of a fully assembled tumor-specific T cell receptor ligated by pMHC. *Cell* **185**, 3201-3213.e19 (2022).
8. Saotome, K. *et al.* Structural analysis of cancer-relevant TCR-CD3 and peptide-MHC complexes by cryoEM. *Nat. Commun.* **14**, 2401 (2023).
9. Xu, C. *et al.* Regulation of T Cell Receptor Activation by Dynamic Membrane Binding of the CD3ε Cytoplasmic Tyrosine-Based Motif. *Cell* **135**, 702–713 (2008).
10. Zhang, H., Cordoba, S.-P., Dushek, O. & Anton van der Merwe, P. Basic residues in the T-cell receptor ζ cytoplasmic domain mediate membrane association and modulate signaling. *Proc. Natl. Acad. Sci.* **108**, 19323–19328 (2011).

535 11. James, J. R. & Vale, R. D. Biophysical Mechanism of T Cell Receptor Triggering in a
536 Reconstituted System. *Nature* **487**, 64–69 (2012).
537 12. Minguet, S., Swamy, M., Alarcón, B., Luescher, I. F. & Schamel, W. W. A. Full activation
538 of the T cell receptor requires both clustering and conformational changes at CD3. *Immunity*
539 **26**, 43–54 (2007).
540 13. Gil, D., Schamel, W. W. A., Montoya, M., Sánchez-Madrid, F. & Alarcón, B. Recruitment
541 of Nck by CD3 epsilon reveals a ligand-induced conformational change essential for T cell
542 receptor signaling and synapse formation. *Cell* **109**, 901–912 (2002).
543 14. Natarajan, K. *et al.* An allosteric site in the T-cell receptor Cβ domain plays a critical
544 signalling role. *Nat. Commun.* **8**, 15260 (2017).
545 15. Rangarajan, S. *et al.* Peptide-MHC (pMHC) binding to a human antiviral T cell receptor
546 induces long-range allosteric communication between pMHC- and CD3-binding sites. *J. Biol.*
547 *Chem.* **293**, 15991–16005 (2018).
548 16. Das, D. K. *et al.* Force-dependent transition in the T-cell receptor β-subunit allosterically
549 regulates peptide discrimination and pMHC bond lifetime. *Proc. Natl. Acad. Sci.* **112**, 1517–
550 1522 (2015).
551 17. Wu, W., Shi, X. & Xu, C. Regulation of T cell signalling by membrane lipids. *Nat. Rev.*
552 *Immunol.* **16**, 690–701 (2016).
553 18. Wang, F., Beck-García, K., Zorzin, C., Schamel, W. W. A. & Davis, M. M. Inhibition of T
554 cell receptor signaling by cholesterol sulfate, a naturally occurring derivative of membrane
555 cholesterol. *Nat. Immunol.* **17**, 844–850 (2016).
556 19. Notti, R. Q. & Walz, T. Native-like environments afford novel mechanistic insights into
557 membrane proteins. *Trends Biochem. Sci.* (2022).

558 20. Robbins, P. F. *et al.* A Pilot Trial Using Lymphocytes Genetically Engineered with an NY-
559 ESO-1–Reactive T-cell Receptor: Long-term Follow-up and Correlates with Response. *Clin.*
560 *Cancer Res.* **21**, 1019–1027 (2015).
561 21. Ulmschneider, M. B. & Sansom, M. S. P. Amino acid distributions in integral membrane
562 protein structures. *Biochim. Biophys. Acta BBA - Biomembr.* **1512**, 1–14 (2001).
563 22. Swamy, M. *et al.* A Cholesterol-Based Allostery Model of T Cell Receptor
564 Phosphorylation. *Immunity* **44**, 1091–1101 (2016).
565 23. Su, Q. *et al.* Cryo-EM structure of the human IgM B cell receptor. *Science* **377**, 875–880
566 (2022).
567 24. Gao, X., Dong, X., Li, X., Liu, Z. & Liu, H. Prediction of disulfide bond engineering sites
568 using a machine learning method. *Sci. Rep.* **10**, 10330 (2020).
569 25. Liu, F., van Breukelen, B. & Heck, A. J. R. Facilitating Protein Disulfide Mapping by a
570 Combination of Pepsin Digestion, Electron Transfer Higher Energy Dissociation (EThcD), and
571 a Dedicated Search Algorithm SlinkS*. *Mol. Cell. Proteomics* **13**, 2776–2786 (2014).
572 26. Yin, Y., Wang, X. X. & Mariuzza, R. A. Crystal structure of a complete ternary complex of
573 T-cell receptor, peptide-MHC, and CD4. *Proc. Natl. Acad. Sci. U. S. A.* **109**, 5405–5410
574 (2012).
575 27. Hawse, W. F. *et al.* Cutting Edge: Evidence for a Dynamically Driven T Cell Signaling
576 Mechanism. *J. Immunol.* **188**, 5819–5823 (2012).
577 28. Lanz, A.-L. *et al.* Allosteric activation of T cell antigen receptor signaling by quaternary
578 structure relaxation. *Cell Rep.* **36**, 109375 (2021).
579 29. Kim, S. T. *et al.* The αβ T Cell Receptor Is an Anisotropic Mechanosensor *. *J. Biol.*
580 *Chem.* **284**, 31028–31037 (2009).

581 30. Fernandes, R. A. *et al.* T Cell Receptors are Structures Capable of Initiating Signaling in
582 the Absence of Large Conformational Rearrangements*. *J. Biol. Chem.* **287**, 13324–13335
583 (2012).
584 31. Reinherz, E. L., Hwang, W. & Lang, M. J. Harnessing αβ T cell receptor mechanobiology
585 to achieve the promise of immuno-oncology. *Proc. Natl. Acad. Sci.* **120**, e2215694120
586 (2023).
587 32. Stewart-Jones, G. B. E. *et al.* Trimeric HIV-1-Env Structures Define Glycan Shields from
588 Clades A, B, and G. *Cell* **165**, 813–826 (2016).
589 33. Lee, J. H., de Val, N., Lyumkis, D. & Ward, A. B. Model Building and Refinement of a
590 Natively Glycosylated HIV-1 Env Protein by High-Resolution Cryoelectron Microscopy.
591 *Structure* **23**, 1943–1951 (2015).
592 34. Chouaki Benmansour, N. *et al.* Phosphoinositides regulate the TCR/CD3 complex
593 membrane dynamics and activation. *Sci. Rep.* **8**, 4966 (2018).
594 35. Costello, P. S., Gallagher, M. & Cantrell, D. A. Sustained and dynamic inositol lipid
595 metabolism inside and outside the immunological synapse. *Nat. Immunol.* **3**, 1082–1089
596 (2002).
597 36. Xu, S. *et al.* Uptake of oxidized lipids by the scavenger receptor CD36 promotes lipid
598 peroxidation and dysfunction in CD8+ T cells in tumors. *Immunity* **54**, 1561-1577.e7 (2021).
599 37. Kent, A., Longino, N. V., Christians, A. & Davila, E. Naturally Occurring Genetic
600 Alterations in Proximal TCR Signaling and Implications for Cancer Immunotherapy. *Front.*
601 *Immunol.* **12**, (2021).
602 38. Klebanoff, C. A., Chandran, S. S., Baker, B. M., Quezada, S. A. & Ribas, A. T cell
603 receptor therapeutics: immunological targeting of the intracellular cancer proteome. *Nat. Rev.*
604 *Drug Discov.* **22**, 996–1017 (2023).

605 39. Chen, J.-L. *et al.* Structural and kinetic basis for heightened immunogenicity of T cell
606 vaccines. *J. Exp. Med.* **201**, 1243–1255 (2005).

607

608

609 **Figures and Legends**

610 **Figure 1**

611

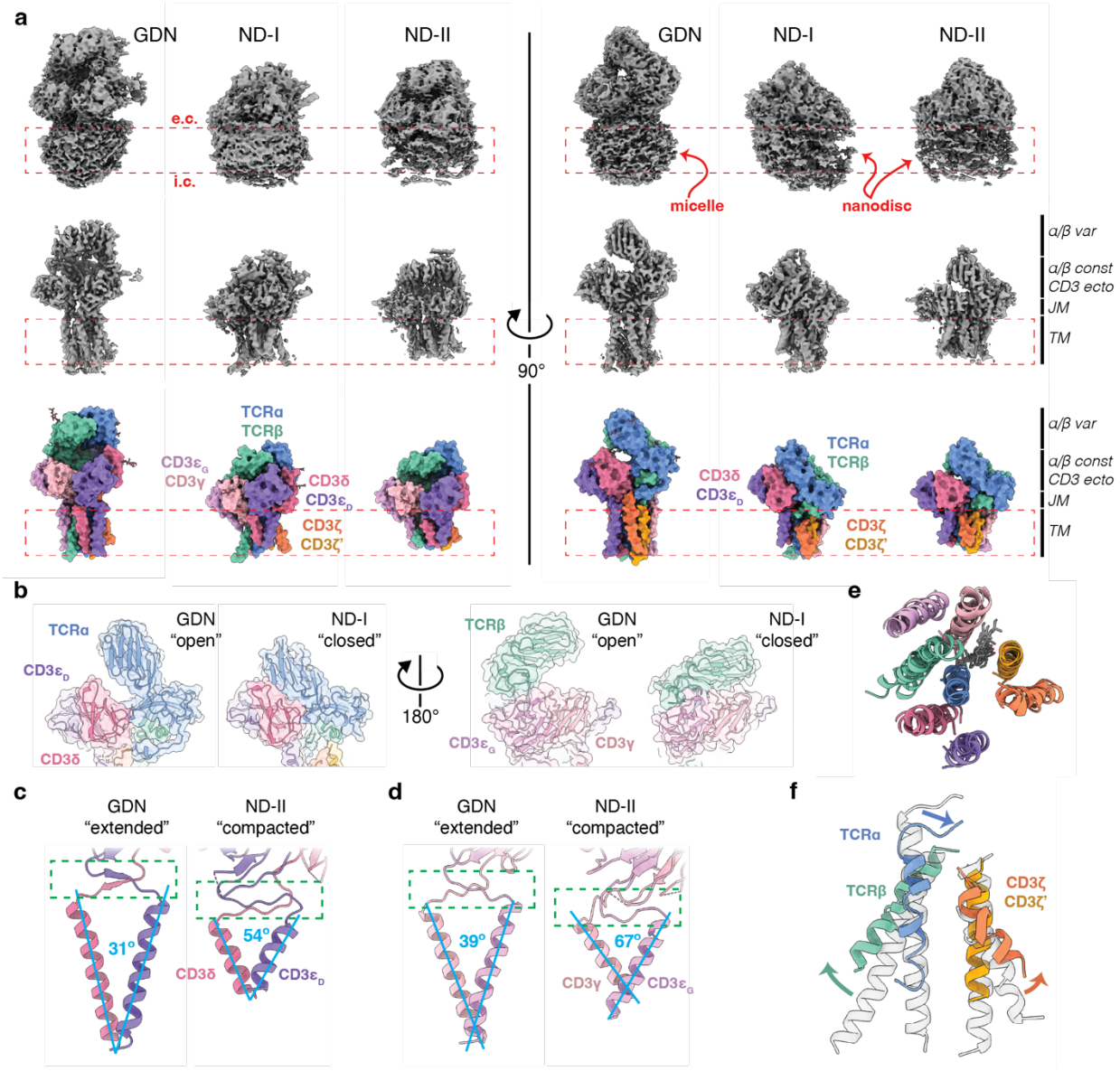

612

613

614 **Figure 1: Architecture of the TCR–CD3 in a native-like lipid environment.** (a) Cryo-EM
615 maps (top, middle) and space-filling solvent-excluded surfaces for the models (bottom; herein,
616 model surfaces) of the TCR–CD3 in a detergent micelle (GDN) and in nanodiscs (conformations
617 ND-I and ND-II). Top row shows cryo-EM density (without local refinement) after B-factor
618 sharpening, contoured to a low threshold to highlight micelle and nanodisc positioning. Red
619 dashed box indicates approximate plasma membrane span as inferred from the micelle and
620 nanodisc densities (red arrows and labels). Extracellular and intracellular faces indicated as e.c.
621 and i.c., respectively. Middle row shows DeepEMhancer-sharpened maps after local refinement,
622 accentuating the protein and glycan densities. Protein regions indicated at far right abbreviated
623 as follows: var, variable domains; ecto, ectodomains; const, constant domains; JM,
624 juxtamembrane linkers; TM, transmembrane helices. (b) Comparison of GDN and ND-I models,
625 highlighting ectodomain closure in the context of a lipid bilayer. Model backbone cartoon inside
626 transparent model surfaces shown. (c,d) Comparison of GDN and ND-II models, highlighting
627 juxtamembrane linker compaction in the direction normal to the lipid bilayer (green dashed box)
628 and coincident splay of the TM helices (cyan lines and angular measures). The CD3$\varepsilon\delta$ and
629 CD3$\varepsilon\gamma$ heterodimers are shown in (c) and (d), respectively. (e) Overlay of the TM helices in the
630 detergent micelle and lipid bilayer (both ND-I and ND-II), viewed from the extracellular space
631 showing similar overall arrangement. (f) Comparison of GDN (transparent gray) and ND-II (solid,
632 color-coded) transmembrane helices aligned to TCRα residues 245-260 and viewed parallel to
633 the membrane. Green and orange arrows highlight increased splay of the TCRβ
634 transmembrane helix and the carboxy-terminal end of the CD3ζ TM helix, respectively. Blue
635 arrow highlights the unstructuring and deflection of the first helical turn at the amino-terminus of
636 the TCRα transmembrane helix in the lipid bilayer.
637

638 **Figure 2**

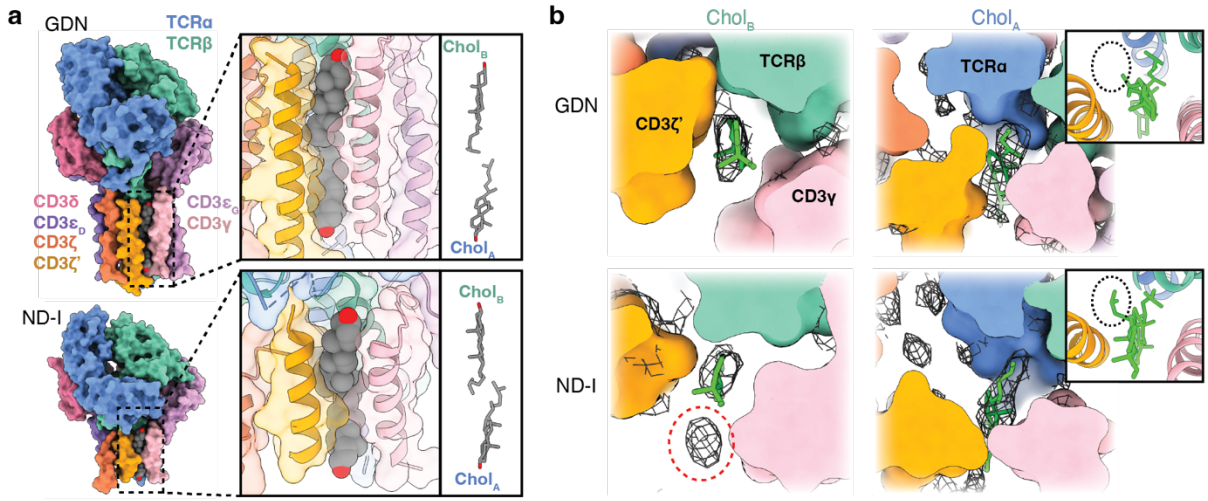

639
640
641

642 **Figure 2: TCR–CD3–lipid interactions.** (a) Comparison of the cholesterol-binding sites of the
643 TCR in detergent (top) and in nanodiscs (bottom). Overview shown at left and insets show the
644 cholesterol-binding sites in detail (left) and with protein removed (right) to highlight the deflection
645 of the branched aliphatic tails. $Chol_B$ denotes the cholesterol proximal to the ectodomains and
646 the TCRβ transmembrane helix; $Chol_A$ denotes the cholesterol proximal to the cytoplasmic face
647 and the TCRα transmembrane helix. (b) Sections parallel to the membrane plane highlighting
648 the opening of the cholesterol-binding groove to the lipid environment in nanodiscs relative to
649 that in detergent. Sections are shown at the levels of $Chol_A$ and $Chol_B$, as indicated. Density
650 from locally refined and B-factor-sharpened cryo-EM maps is shown as black mesh, and
651 cholesterols in lime green. Red dashed circle highlights structured lipid density in the nanodisc
652 bilayer adjacent to the opened cholesterol-binding groove. Insets show the cholesterol-binding
653 groove from the same angle as the main panels, but with both cholesterols shown in the slice,
654 highlighting intercalation of the deflected $Chol_B$ aliphatic chain between TM helices in nanodiscs
655 (black dashed oval) as compared to the structure in GDN.
656
657

658 **Figure 3**

659

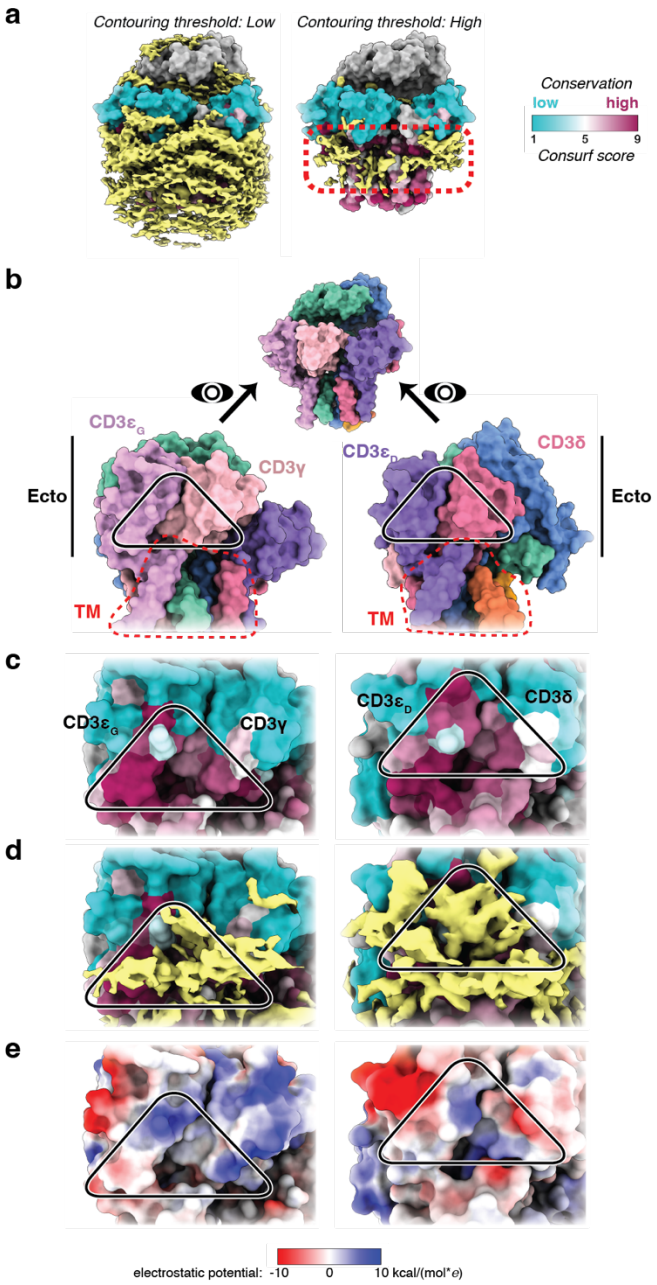

660
661
662

Figure 3: Conserved CD3 surface patches form extensive membrane contacts. (a) ND-II model surface colored by sequence conservation (Consurf score 1 through 9) and yellow unmodeled map density from the nanodisc enshrouding the TCR–CD3 TM helices and membrane-proximal ectodomain surfaces. When visualized with a higher contouring threshold (right), structured lipid density adjacent to the CD3 ectodomains persisted (red dotted box). Note also the relative sequence conservation in the CD3 TM helices and membrane-adjacent ectodomain surfaces, but not solvent-exposed surfaces. (b) Top, ND-II space-filling model for orientation. Arrows and eyes indicate the viewing direction for inspection of the CD3εγ and CD3εδ interfaces examined in the lower panels. Bottom, overviews orienting the close-up views in panels c through e. Red dashed lines denote the border between TM and ectodomain (Ecto) surfaces. (c) Close-up views of the membrane-proximal face of the CD3 heterodimers, with black triangles highlighting the conserved surface patch at the subunit interface. (d) Lipid density (yellow) is most robust over this conserved patch, visualized at high contouring threshold (as in panel a, right). (e) The conserved ectodomain patch is relatively electropositive compared to the surrounding ectodomain surfaces colored by electrostatic potential (red to blue, -10 to 10 kcal/(mol*e)).

681 **Figure 4**

682

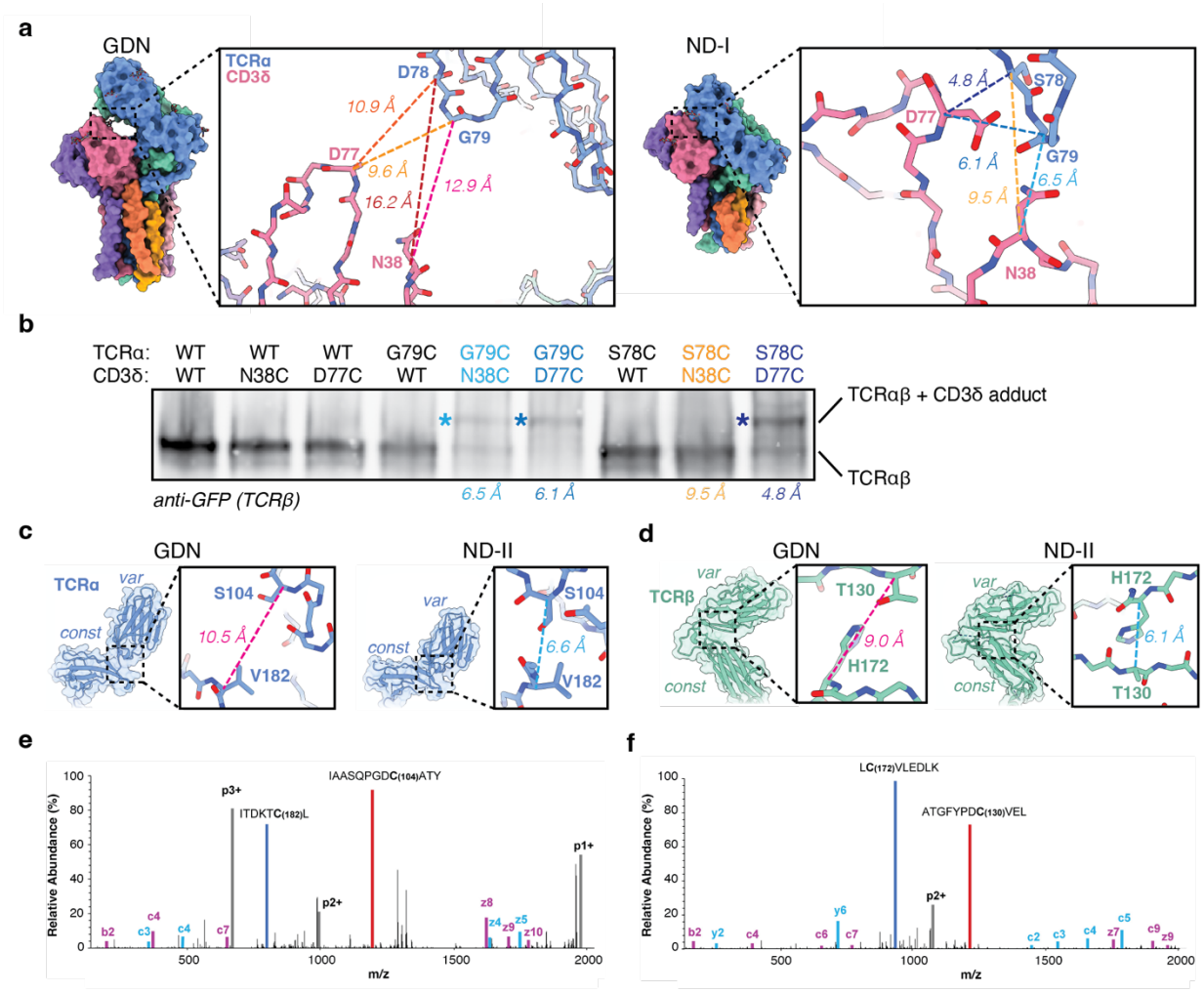

683

684 **Figure 4: Confirmation of the TCR–CD3 resting conformation *in situ.*** (a) Comparison of
685 Cα-Cα distances between apposing faces of CD3δ and TCRα in detergent and in a lipid bilayer,
686 highlighting plausible engineered disulfide positions in ND-I (distances in blue shades) that are
687 not geometrically plausible in GDN (distances in yellow, orange, red, magenta). (b) Non-
688 reducing SDS-PAGE gel of whole-cell lysates from HEK293T cells infected with the indicated
689 TCR–CD3 virus genotypes Western blotted for EGFP-tagged TCRβ. Engineered disulfides
690 yielding a TCRαβ–CD3δ covalent adduct resulted in an upward gel shift (asterisks). Color
691 coding and distances as in panel a. (c,d) Design of intrachain disulfides in the closed
692 conformation of TCRα (c) and TCRβ (d). Distances color coded as above. (e,f) Mass
693 spectrometric detection of intrachain disulfides in TCRα (e) and TCRβ (f). EThcD fragment
694 spectra of disulfide-linked dipeptides are shown. Gas-phase reduced linear peptides are shown
695 in red (peptide A) and blue (peptide B) with the reduced Cys highlighted in bold. Fragment ions
696 of the two linear peptides are shown in magenta (fragments of peptide A) and cyan (fragments
697 of peptide B). Charge-reduced precursor ions are shown in gray.
698
699

700 **Figure 5**
701

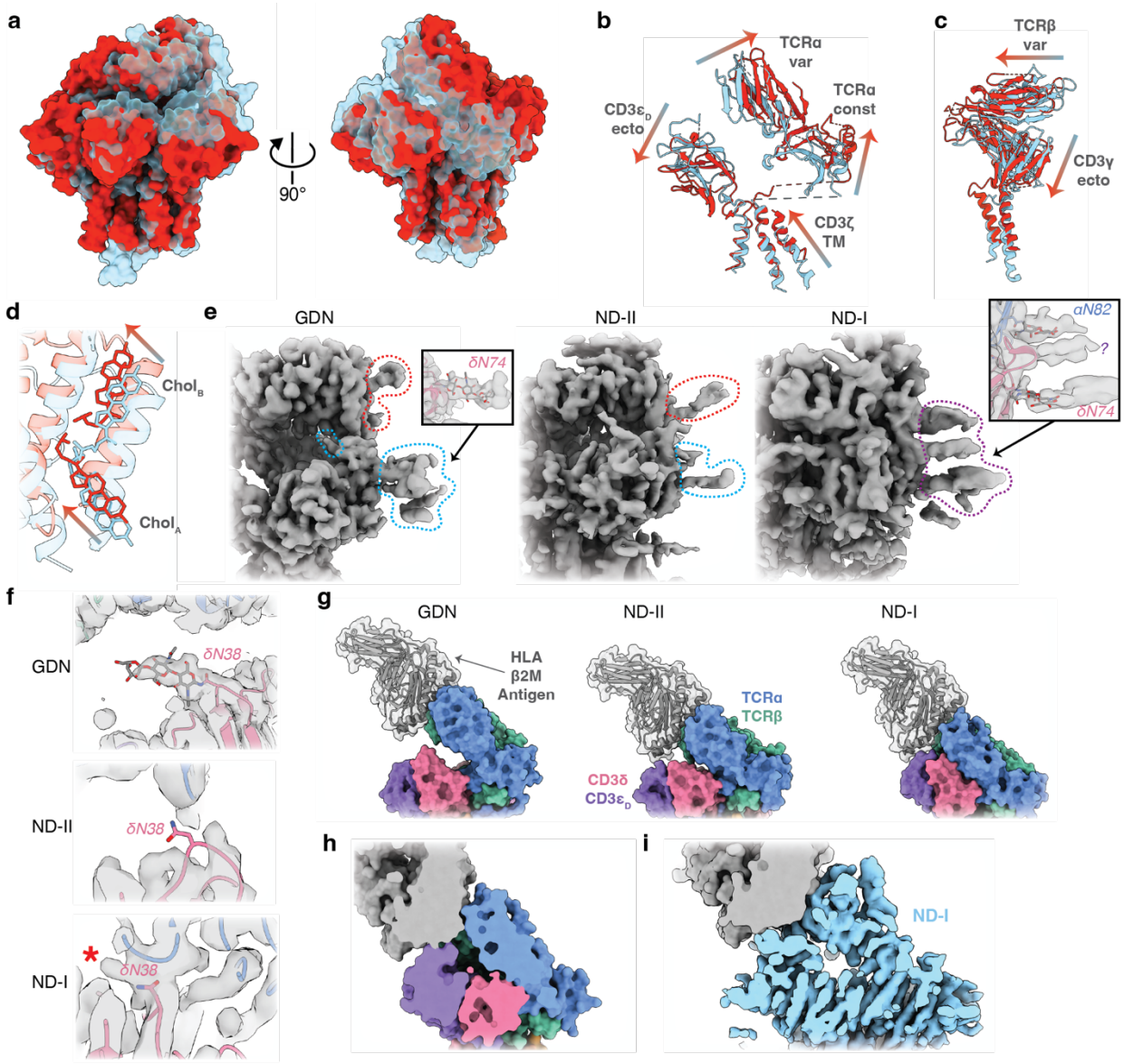

702
703
704
705

706 **Figure 5: Basal conformational variability of the TCR–CD3.** (a) Comparison of ND-I
707 (transparent cyan) and ND-II (red), shown here as model surfaces, aligned on the TCRα
708 transmembrane helix. (b,c) Gradient arrows highlight the domain movements underlying the
709 transition between ND-I (cyan) and ND-II (red). (d) TCRβ and CD3γ TM helix movement away
710 from the cholesterol-binding site during the transition from ND-I to ND-II, with arrows indicating
711 the accompanying movements of the cholesterols in the sterol-binding groove. (e) Comparison
712 of the TCRα and CD3δ lateral glycosylation sites (red and cyan dashed lines, respectively) in
713 the density maps showing increasing ordering of the glycan array with ectodomain closure
714 (purple dashed line). Insets highlight modeled asparagine-linked glycan cores (or partial cores)
715 modeled into these densities in GDN and ND-I. (f) Comparison of the CD3δ N38 residue in
716 GDN, ND-II and ND-I. Gray surface is the locally refined, DeepEMhancer-sharpened cryo-EM
717 density. (g) Modeling HLA-β2M-antigen (gray) binding to the TCR in the indicated
718 conformations. (h) Cross section through the HLA–TCR interface in ND-I shows close
719 association of HLA and CD3ε_D, but no large clashes. (i) Similarly, modeling HLA onto the locally
720 refined, DeepEMhancer-sharpened ND-I density does not show any large clashes between HLA
721 and unmodelled density.
722
723

724 **Figure 6**
725

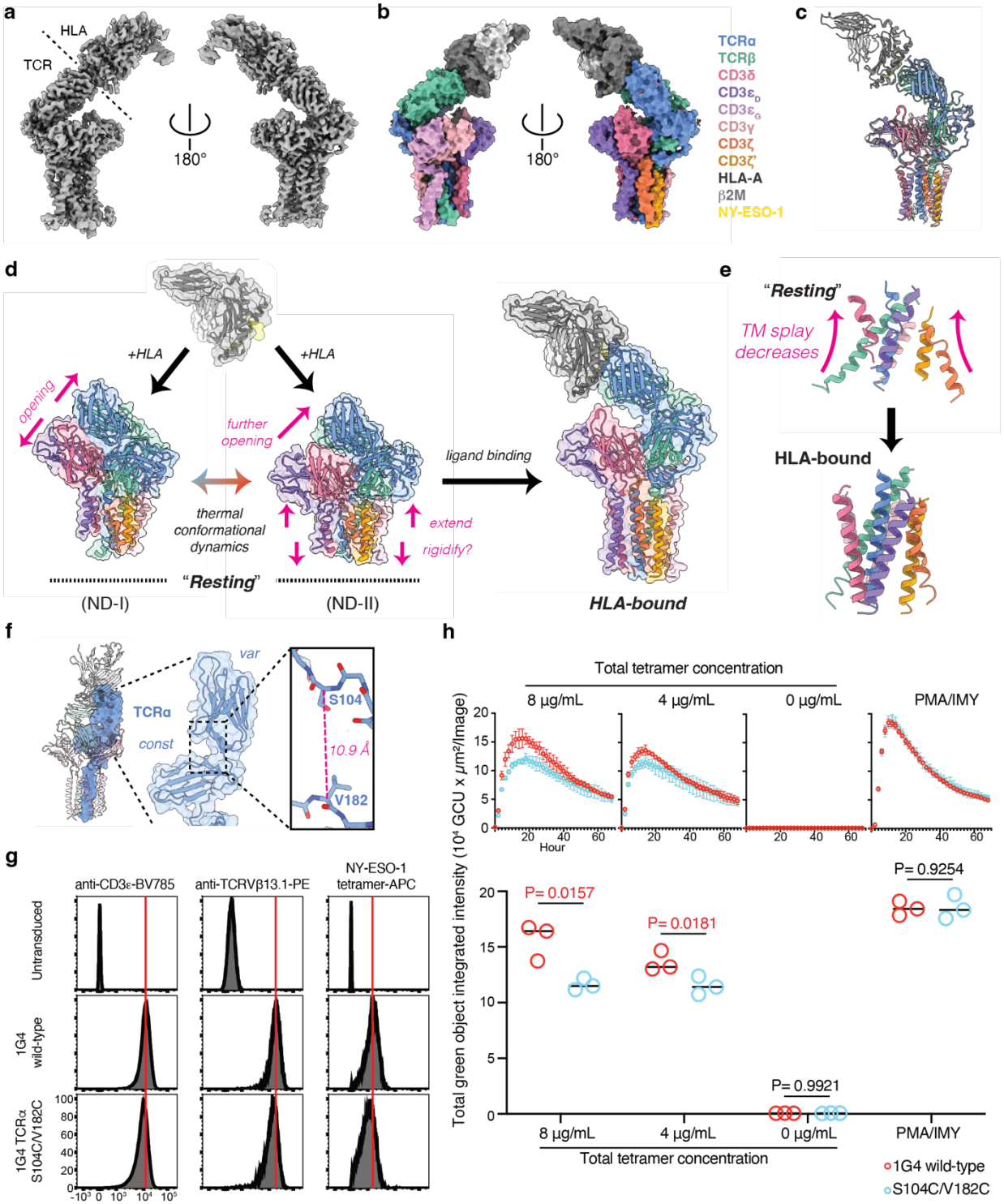

726
727
728
729

730 **Figure 6: Structure of the HLA-bound TCR–CD3 complex in nanodiscs and model of**
731 **TCR–CD3 activation.** (a,b) Cryo-EM maps (a) and model surfaces (b) of HLA-bound TCR–CD3
732 in nanodiscs. Maps shown in (a) were DeepEMhancer-sharpened after local refinement to
733 remove nanodisc density. Legend in (b) applies to (b) – (f). (c) Comparison of GDN and HLA-
734 bound models, highlighting the similarity in TCR–CD3 conformation. HLA-bound model is
735 colored by chain and GDN is transparent gray. (d) Proposed model of TCR–CD3 conformational
736 dynamics. The unliganded TCR–CD3 explores resting subconformations (between ND-I and
737 ND-II). HLA binding induces a conformational transition from ND-II to an open, extended
738 conformation. Magenta arrows and text indicate movements required to transition to the next
739 conformation in the series. (e) Changes in the TM helices between "resting" (ND-I shown) and
740 HLA-bound conformations. (f) Increasingly zoomed-in views of the TCRα variable and constant
741 domains in the HLA-bound conformation highlighting the Cα-Cα distance between S104 and
742 V182. (g) Flow cytometry histogram from J8Zb2m-α-β- cells post tetramer-APC enrichment and
743 stained as indicated (n = 3 replicates). Cells were untransduced (top) or transduced with a virus
744 expressing the TCR$\alpha\beta$ 1G4 genotype indicated (middle, bottom). Vertical axis is cell count
745 normalized to peak; horizontal axis is fluorescence in arbitrary units. Red line indicates
746 fluorescence intensity mode (histogram peak) for wild-type 1G4. (h) Time-dependent T-cell
747 activation quantified using an NFAT-ZsGreen reporter by live cell imaging. Top shows ZsGreen
748 fluorescence over time after addition of indicated concentrations of HLA-tetramer or
749 PMA/ionomycin for 1G4 wild-type (red) or TCRα S104C/V182C mutant-transduced cells (cyan).
750 Data shown are mean +/- standard deviation using biologic triplicates. Peak CD3-TCR
751 activation amplitudes are compared for each condition at the 8 μg/mL HLA-tetramer peak
752 (t=16h) for all HLA-tetramer concentrations or at the PMA/Ionomycin peak (t=10h) specifically

753 for that condition (bottom). P values calculated by unpaired, two-tailed t-test shown for each

754 comparison. $P < 0.05$ highlighted in red.

755

756

757 **Extended Data Figures and Legends**
758
759 **Extended Data Figure 1**
760

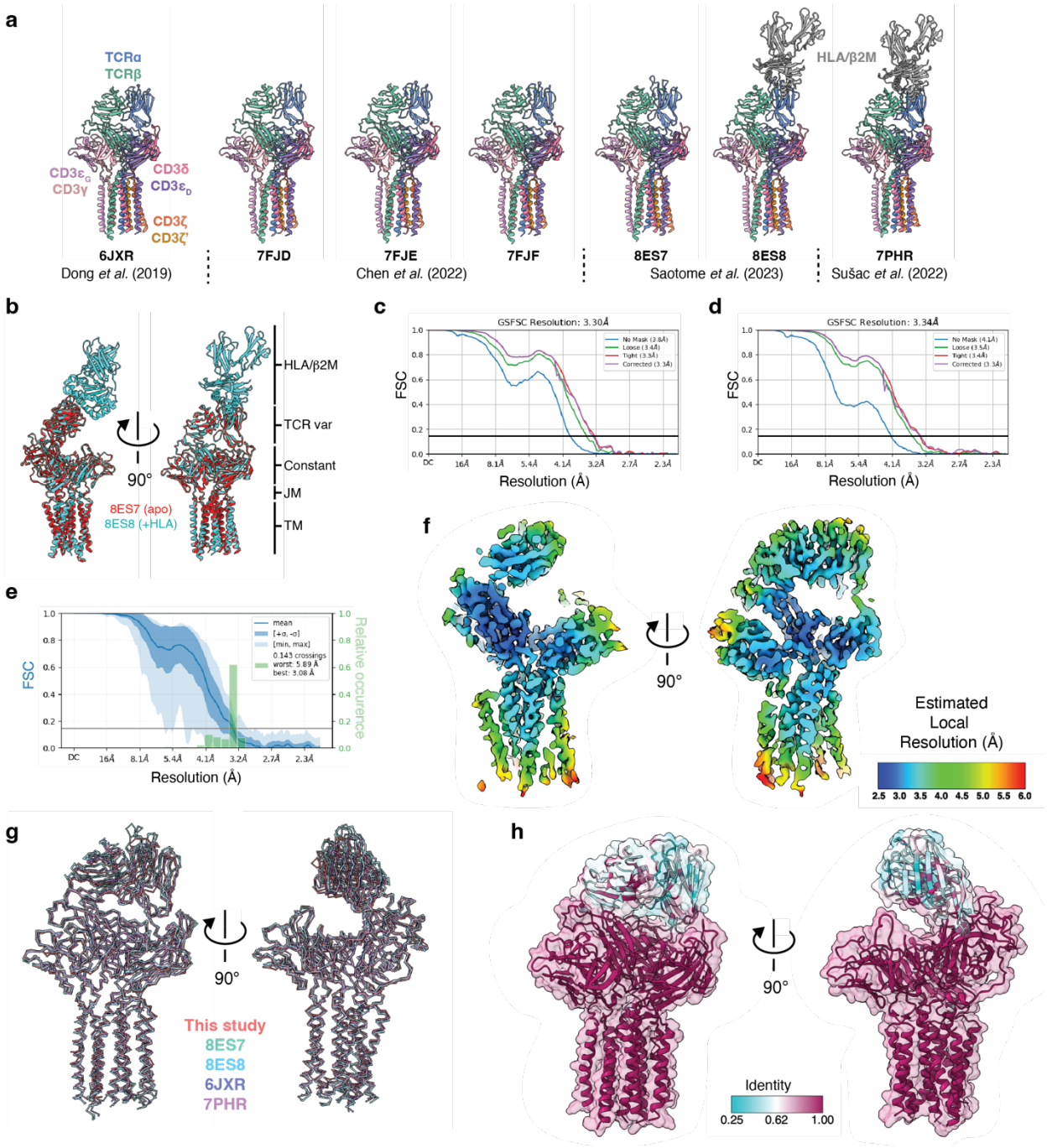

761
762
763
764

765 **Extended Data Figure 1: The TCR–CD3 in detergent.** (a) Cartoon representations of
766 previously published structures of the TCR–CD3 by itself and in complex with HLA-β2M-antigen
767 determined in detergent micelles by cryo-EM. Models are colored by chain as indicated. (b)
768 Superposition of published structures of a TCR–CD3 by itself (red) or in complex with HLA-β2M-
769 antigen (cyan), showing no meaningful structural change throughout the TCR structure upon
770 ligand binding. (c) Gold-standard Fourier shell correlation (FSC) curves for the map of the TCR–
771 CD3 in GDN (herein, simply "GDN") determined in this study after non-uniform refinement. (d)
772 FSC curve for the locally refined GDN map (mask excluded micelle density). While resolution
773 was not nominally improved by masking out the micelle, map interpretability was qualitatively
774 improved, and this map was used for further analysis. (e) Three-dimensional (3D) FSC analysis
775 for the locally refined GDN map, showing relatively little map anisotropy. (f) Central slices of the
776 locally refined GDN map, colored by local resolution estimate, as indicated in the panel. (g)
777 Backbone representation of the GDN structure compared with those of TCR–CD3 sequences
778 previously determined in other studies. Models containing HLA-β2M-antigen have had those
779 atoms removed for this analysis. (h) GDN model colored according to sequence identity among
780 the four TCR–CD3 sequences (this study and three priors) with cryo-EM structures determined
781 in detergent micelles.
782
783

Extended Data Figure 2

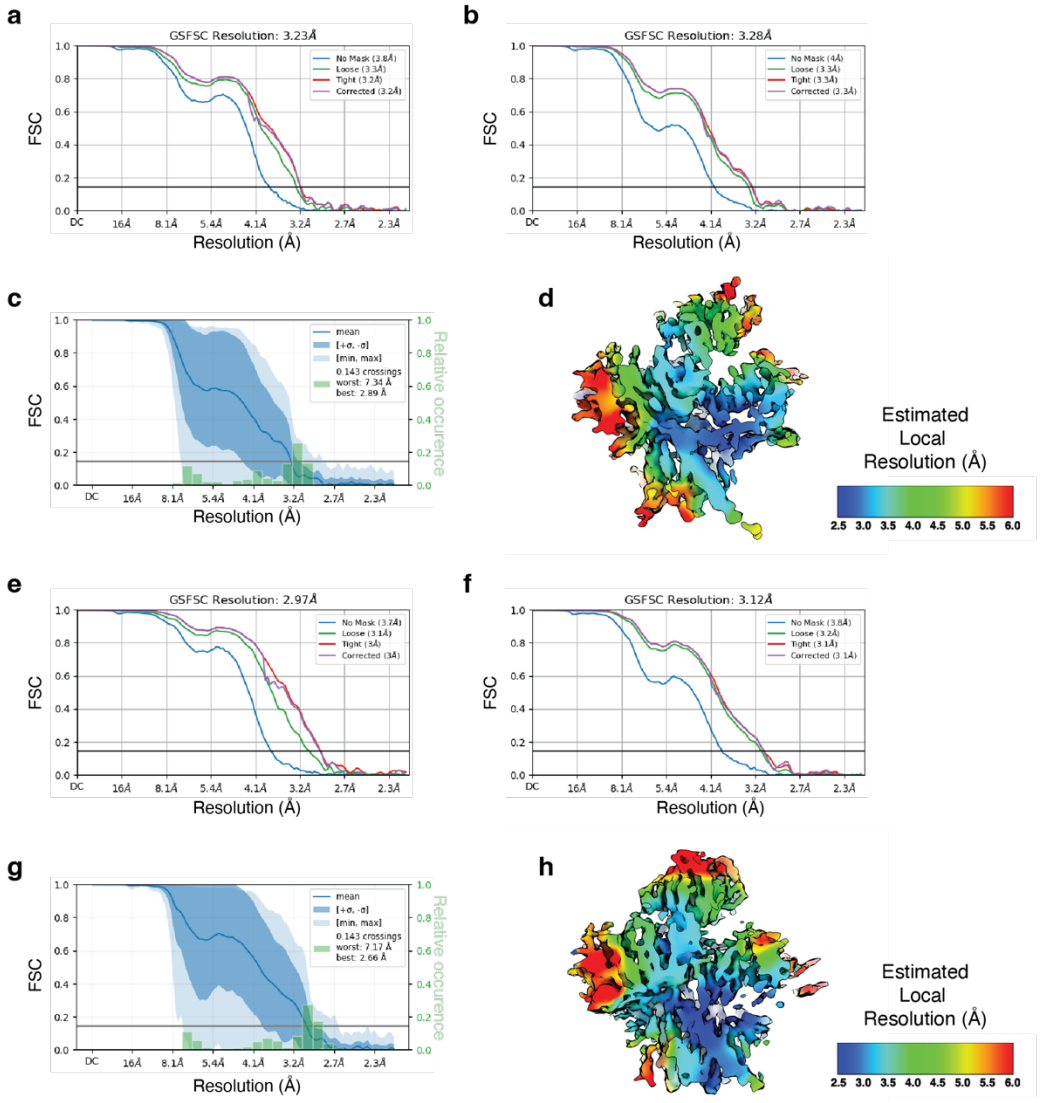

Extended Data Figure 2: Map assessment for ND-I and ND-II. (a) Gold-standard FSC curves for the ND-I map after non-uniform refinement. (b) FSC curves for the locally refined ND-I map (mask excluded nanodisc density). While resolution was not nominally improved by masking out the nanodisc, map interpretability was qualitatively improved, and this map was used for further analysis. (c) 3D FSC analysis for locally refined ND-I. Note the more extensive anisotropy than was seen for the TCR–CD3 in detergent micelles. (d) Central slice of locally refined ND-I, colored by local resolution estimate, as indicated in the panel. (e) Gold-standard FSC curves for the ND-II map after non-uniform refinement. (f) FSC curves for the locally refined ND-II map (mask excluded nanodisc density). As with ND-I, nominal resolution was not improved by masking out the nanodisc, but map interpretability was qualitatively improved, and this map was used for further analysis. (g) 3D FSC analysis for locally refined ND-II. Note again the more extensive anisotropy than was seen for the TCR in detergent micelles. (h) Central slice of locally refined ND-II, colored by local resolution estimate, as indicated in the panel.

Extended Data Figure 3

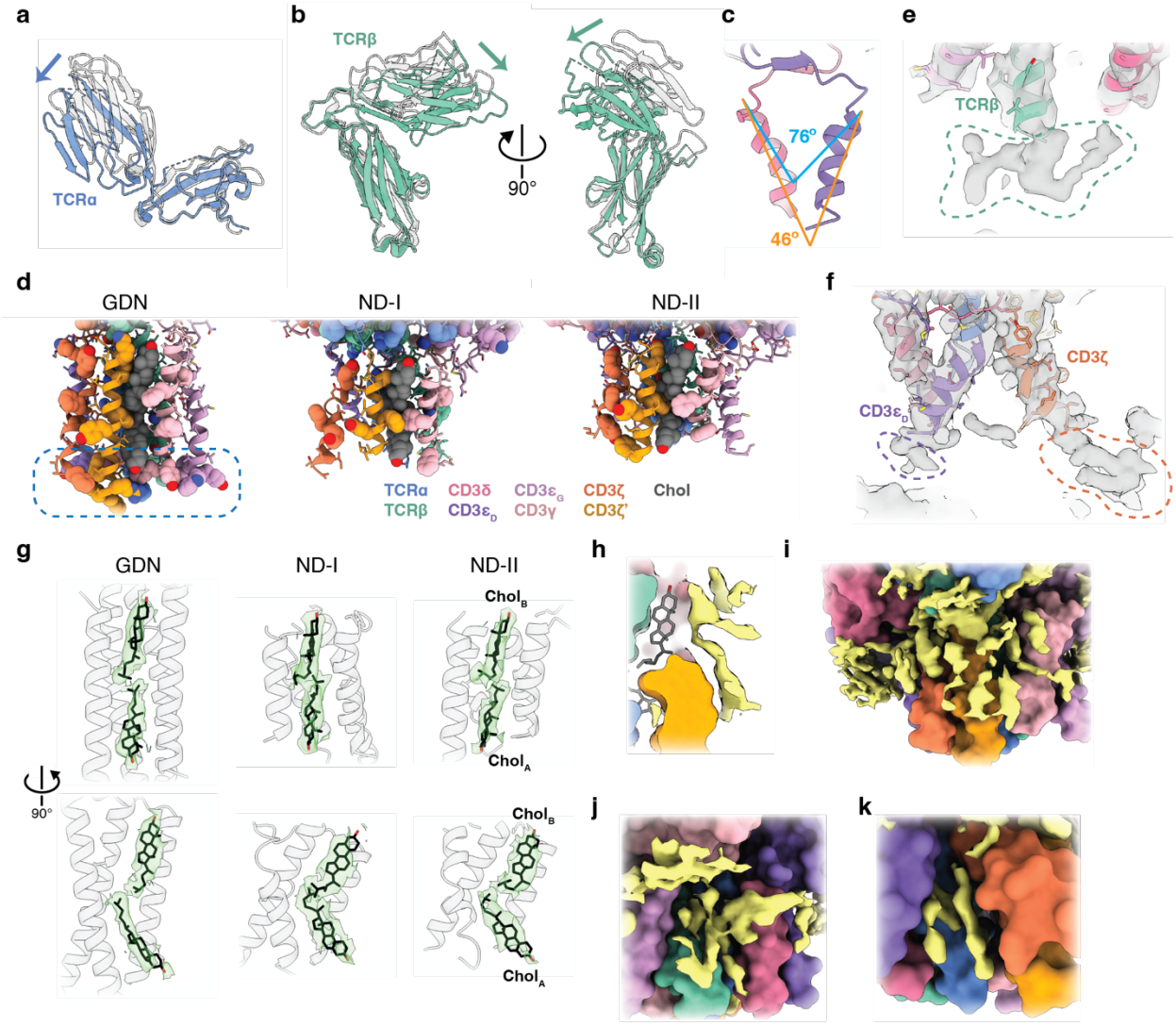

811 **Extended Data Figure 3: Structural detail of the TCR–CD3 in nanodiscs.** (a,b) Cartoon
812 representations of ND-I (solid) and GDN (transparent gray) TCRα (panel a) and TCRβ (panel b),
813 aligned to the respective TCR constant domains. Arrows indicate the movements of the variable
814 domains relative to the constant domains that comprise the "closure" of the variable domains in
815 ND-I/II relative to GDN. (c) The bent TM helices of the ND-I CD3ε_D heterodimer. Splay
816 measured at the level of the first helical turn (cyan) is greater than that of the helices overall
817 (orange). (d) Cartoon representation of the indicated models with basic and aromatic residues
818 highlighted as space-filling spheres. Blue dashed box highlights the clusters of basic and
819 aromatic residues modeled at the carboxy-termini of the TM helices in GDN, but unstructured in
820 ND-I and ND-II. Color legend applies to all figure panels. (e,f) Density projecting from the
821 carboxy-termini of the TM helices modeled in ND-II that could not be confidently modeled, but
822 likely corresponding to continuation of the polypeptide chains. Gray, DeepEMhancer-sharpened
823 maps. Dashed lines encircle the densities in question. (g) Density corresponding to the
824 cholesterols modeled in ND-I, ND-II, and GDN. The transparent green surface is the indicated
825 locally refined, B-factor-sharpened cryo-EM map, cropped to a zone of 2.2 Å around the
826 cholesterols (black). (h-k) Additional densities likely attributable to lipids in the ND-II map.
827 Proteins are shown as model surfaces, and cholesterol in stick representation. Yellow surface is
828 the ND-II B-factor-sharpened map after local refinement (h) or non-uniform refinement (i-k) with
829 the modeled densities subtracted to highlight unmodeled densities.
830
831

832 **Extended Data Figure 4**

833

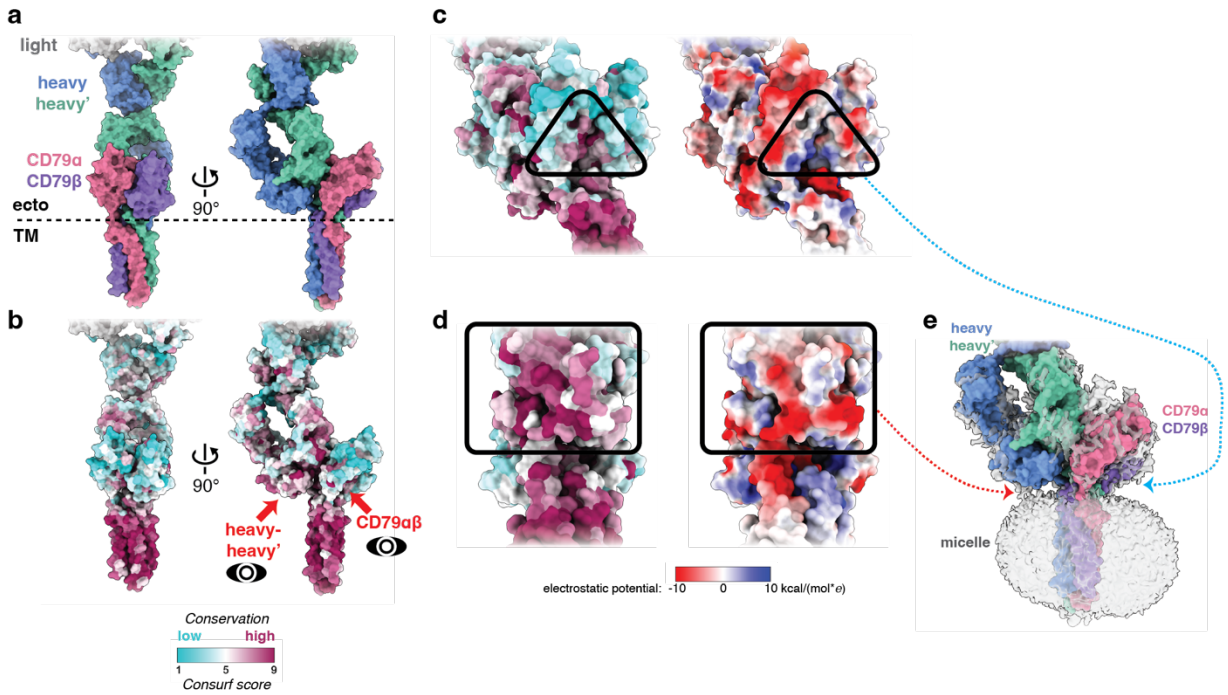

834
835
836
837

838 **Extended Data Figure 4: Insights into BCR structure and membrane interaction.** (a,b)
839 Surface representation of the human B-cell receptor (BCR) model, as determined in a detergent
840 micelle by cryo-EM (PDB 7XQ8)[23]. The model is colored by chain (a) and by sequence
841 conservation (b, scale applies to remainder of figure). Red arrows and eye icons labeled
842 CD79αβ and heavy-heavy' indicate the direction for the magnified views in panels (c) and (d),
843 respectively. (c) Membrane-proximal face of the CD79αβ interface, colored by conservation
844 (left, as in panel a) and electrostatic potential (right). Black triangle highlights region of high
845 sequence conservation and corresponding surface electropositivity. However, this patch is
846 oriented away from the micelle surface in the structure in detergent (dashed arrow to panel e).
847 (d) Membrane-proximal face of the IgM heavy chains, with black box highlighting broad
848 sequence conservation and largely electronegative conserved face. Dashed arrow indicates
849 contact between this surface patch and the detergent micelle density in panel e. Electrostatic
850 potential scale applies to panels c and d. (e) Surface model of the BCR with the unmodeled
851 map density shown (transparent gray). Note the detergent micelle enshrouding the TM helices
852 and making contact with the electronegative heavy-heavy' interface (red dashed arrow) but not
853 the electropositive CD79αβ interface (blue dashed arrow), which is the opposite of what might
854 be expected in a phospholipid membrane.
855
856

857 **Extended Data Figure 5**

858

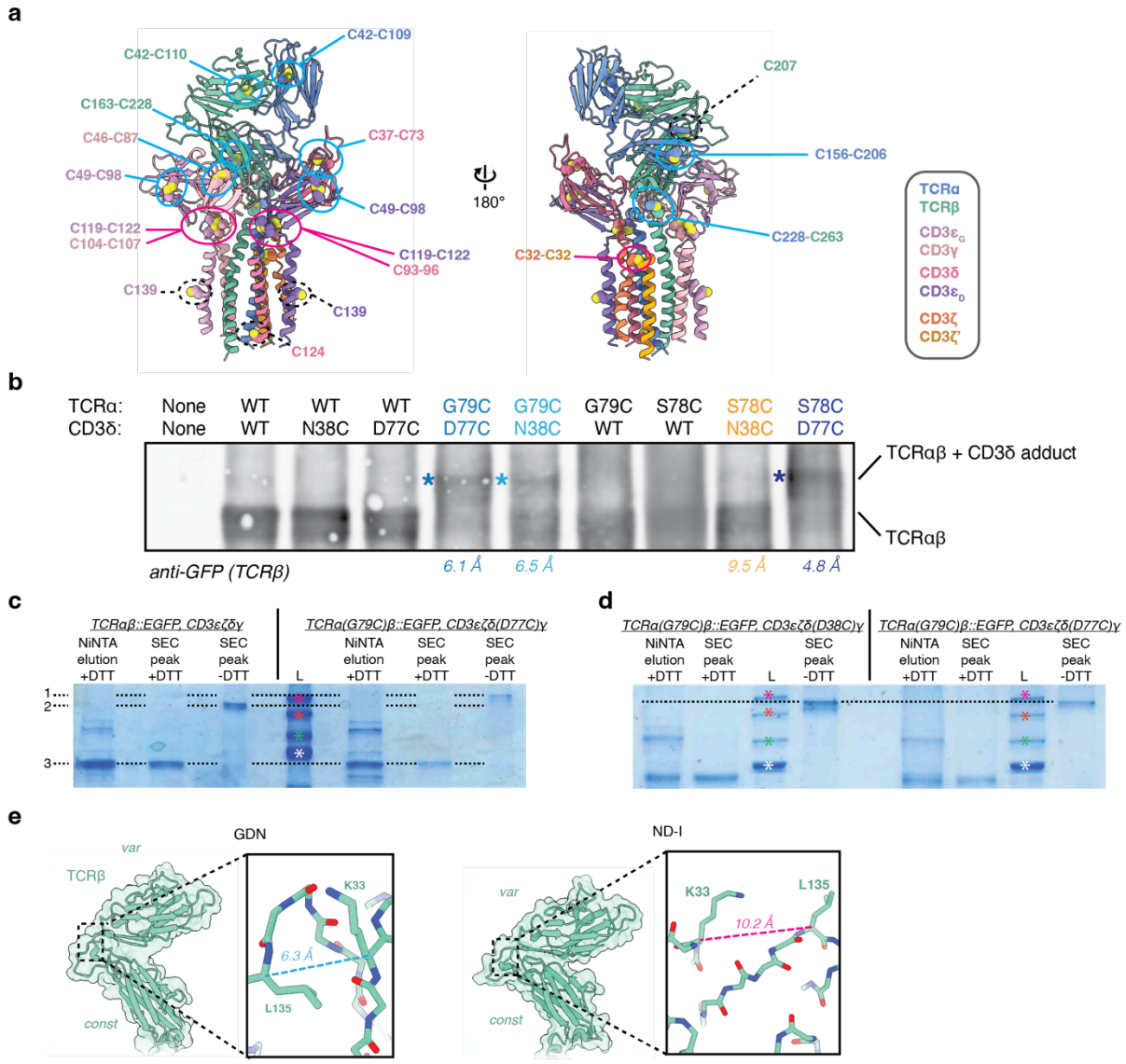

859
860
861
862

863 **Extended Data Figure 5: Engineered disulfide crosslinking.** (a) Location of all native
864 disulfides (solid cyan and magenta ovals) and unpaired cysteines (dashed black ovals) in the
865 used TCR constructs. Disulfides indicated by cyan ovals are amenable to mass spectrometric
866 detection as peptide pairs after EThcD, whereas disulfides indicated by magenta ovals are not
867 unambiguously detectable by this approach, as they are C-X-X-C lariats or symmetric between
868 CD3ζ homodimers. Subunits colored as indicated to the right. (b) Non-reducing SDS-PAGE gel
869 of NiNTA affinity-purified TCR complex from HEK293T cells infected with the indicated TCR
870 virus genotypes and Western blotted for EGFP-tagged TCRβ. Engineered disulfides yielding a
871 TCRαβ–CD3δ covalent adduct results in an upward gel shift (asterisks). Color coding and
872 distances as in Figure 4a,b. (c,d) Acquastain-stained SDS-PAGE gels of NiNTA affinity-purified
873 TCR complex reconstituted into nanodiscs and purified by size-exclusion chromatography
874 (SEC). Virus genotypes indicated above gels. The presence (+) or absence (-) of reducing
875 agent dithiothreitol (DTT) in the sample-loading buffer is indicated. In panel c, dashed line
876 markers 1, 2, and 3 indicate the inferred electrophoretic mobility of the TCRαβ::EGFP–
877 CD3δ adduct, TCRαβ::EGFP, and TCRβ::EGFP, respectively. Note the mobility shift between
878 the nonreduced wild-type TCR complex and the non-reduced TCRα(G79C)–CD3δ(D77C)
879 mutant complex. Molecular weight ladder (L) is color-coded with magenta, orange, green, and
880 white asterisks denoting 250 kDa, 150 kDa, 100 kDa, and 75 kDa, respectively. In panel d, the
881 non-reduced TCRα(G79C)–CD3δ(D38C) mutant complex displays an electrophoretic mobility
882 similar to that of the non-reduced TCRα(G79C)–CD3δ(D77C) mutant complex, consistent with
883 engineered disulfide formation. (e) Design of an engineered disulfide bond plausible in the GDN
884 conformation but not in the closed ND-I conformation.
885
886
887

Extended Data Figure 6

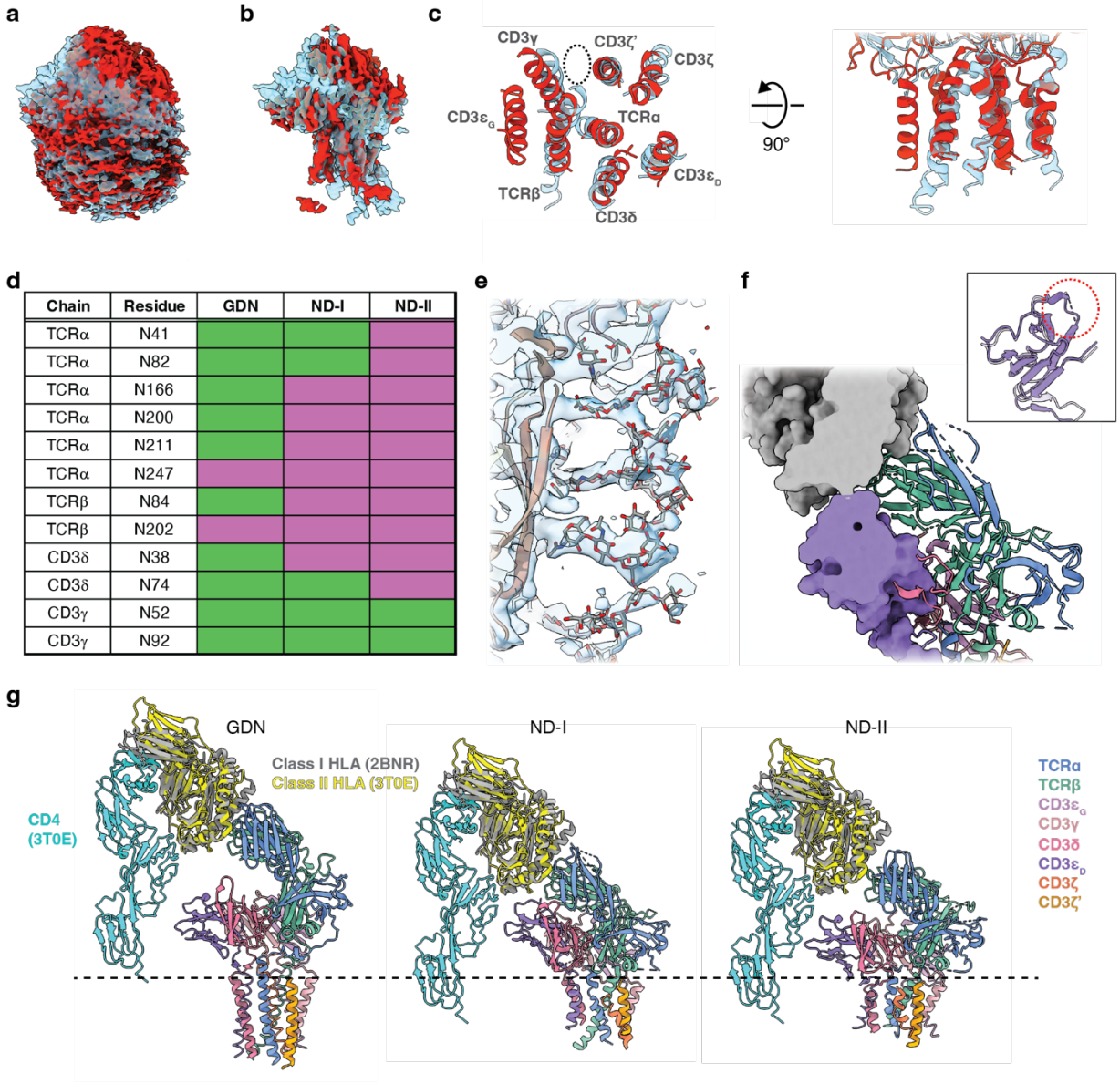

Chain	Residue	GDN	ND-I	ND-II
TCRα	N41			
TCRα	N82			
TCRα	N166			
TCRα	N200			
TCRα	N211			
TCRα	N247			
TCRβ	N84			
TCRβ	N202			
CD3δ	N38			
CD3δ	N74			
CD3γ	N52			
CD3γ	N92			

893 **Extended Data Figure 6: Basal conformational variation and glycosylation of the TCR–**
894 **CD3.** (a,b) Cryo-EM maps for ND-I (transparent cyan) and ND-II (solid red) aligned to the TCRα
895 transmembrane helix. The B-factor-sharpened map without local refinement and
896 DeepEMhancer-sharpened, locally refined maps are shown (a and b, respectively). (c) Relative
897 positions of the TM helices for ND-I and ND-II (colored as in panel a) viewed along the axis
898 perpendicular to the membrane plane (left) and parallel to the membrane (right). Dashed circle
899 indicates cholesterol-binding groove. (d) Graphical representation of partially modeled N-linked
900 glycans in GDN, ND-I, and ND-II. All asparagine residues within an N-X-S/T motif in the
901 structure are included in this list for completeness; however, TCRα N247 is located in the TM
902 domain and is unlikely to undergo glycosylation. Green, modeled; magenta, not modeled. (e)
903 Glycans (gray sticks) in a structured array on the surface of HIV Env as determined by x-ray
904 crystallography (PDB 5FYJ)[32]. Protein shown as cartoon backbone. 2Fo-Fc map contoured to
905 1σ and clipped to within 5 Å of the model. (f) Space-filling model of HLA docked onto ND-I with
906 the CD3ε_D ectodomain from GDN docked in place of that from ND-I, showing minimal, if any
907 steric clashing. Cartoon representation of the remainder of ND-I shown for orientation. Inset
908 shows alignment of CD3ε_D from GDN and ND-I by their ectodomains. Red dashed circle
909 highlights surface loop (residues 107-109) not modeled in ND-I (purple dashed line) but
910 modeled in GDN. (g) Alignment of the CD4–Class II HLA–TCR ternary complex structure (PDB
911 3T0E)[26] to the Class I HLA docked onto our structures as in panel f and Figure 5. The Class II
912 HLA from 3T0E is shown in yellow, and CD4 in cyan. Other color coding as indicated. Dashed
913 black line represents the approximate boundary of the lipid bilayer outer leaflet.
914

915 Extended Data Figure 7

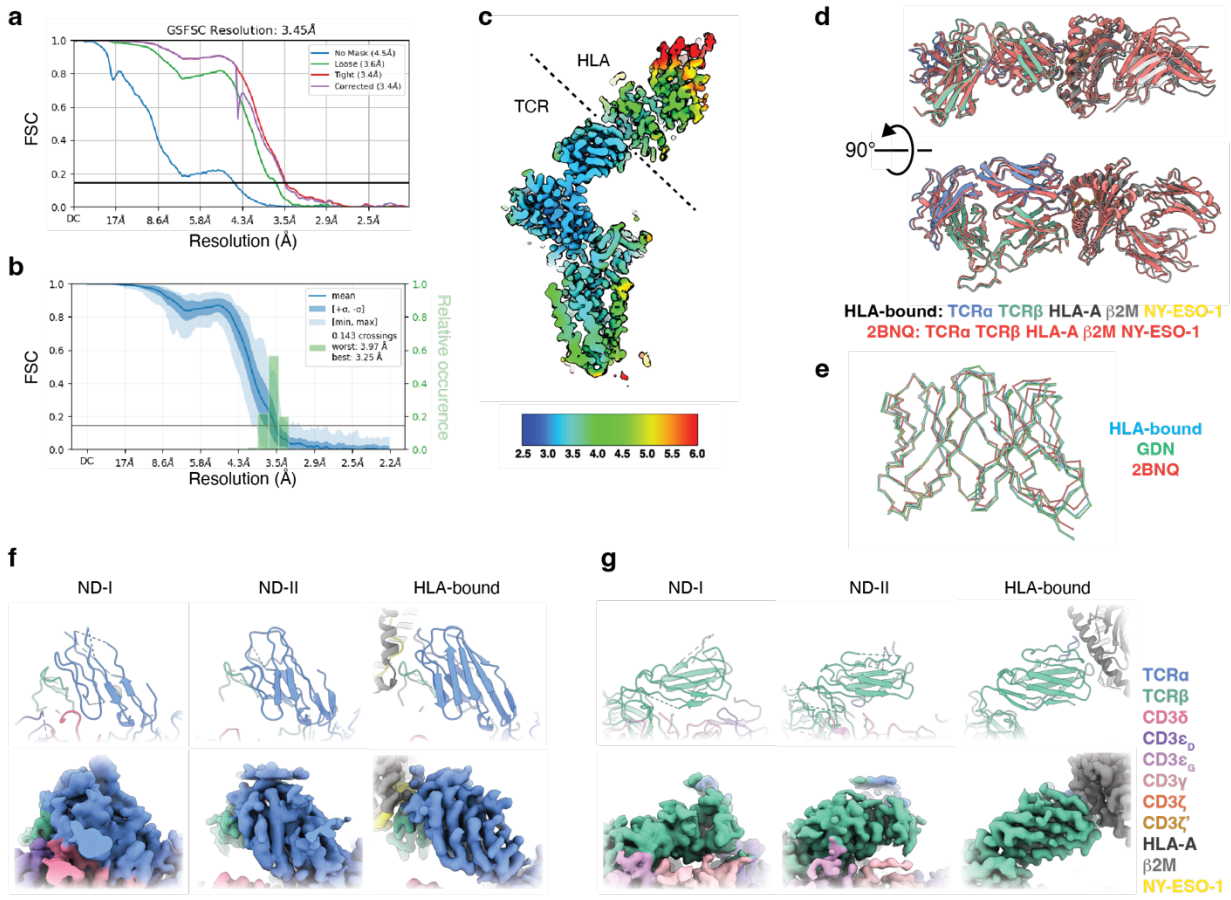

916

917

Extended Data Figure 7: Map assessment and structural analysis of the TCR–CD3 complex in nanodiscs bound to HLA. (a) FSC curves for the locally refined map of HLA-bound TCR–CD3 complex (herein HLA-bound) in nanodiscs. Local refinement mask excluded nanodisc density. (b) 3D FSC analysis for the locally refined HLA-bound map. (c) Central slice of the locally refined HLA-bound map colored by local resolution estimate in Å. (d) Cartoon representation of the TCR variable domains and HLA from the HLA-bound structure (colored by chain) and the NY-ESO-1 TCR–HLA complex crystal structure (2BNQ[39]), colored red. Structures were aligned to the TCR variable domains. (e) Backbone traces of the TCR variable domains from HLA-bound, GDN, and the NY-ESO-1 TCR–HLA complex crystal structure (2BNQ[39]). Structures were aligned to the TCRα variable domain. (f,g) Comparison of the cryo-EM density for the TCR variable domains in HLA-bound and resting state subconformations zoomed on TCRα (f) and TCRβ (g). Top row, cartoon representation of model; bottom row, cryo-EM map. Legend in (g) also applies to (f).

932 **Extended Data Tables**

933

934 **Extended Data Table 1: Model building and refinement statistics.**

	GDN	ND-I	ND-II	HLA-bound
Model				
Composition (#)				
Chains	10	12	10	12
Atoms	8440	6402	6242	10620
Residues	Protein: 1052	Protein: 828	Protein: 821	Protein: 1356
	Nucleotide: 0	Nucleotide: 0	Nucleotide: 0	Nucleotide: 0
Water	0	0	0	0
Ligands	BMA: 3	BMA: 1	BMA: 1	BMA: 1
	NAG: 15	NAG: 9	NAG: 3	NAG: 10
	CLR: 2	CLR: 2	CLR: 2	CLR: 2
Bonds (RMSD)				
Length (Å) (# > 4σ)	0.003 (0)	0.004 (0)	0.003 (0)	0.005 (0)
Angles (degrees) (# > 4σ)	0.923 (6)	0.862 (6)	0.906 (3)	0.892 (15)
MolProbity score	1.9	2.74	2.67	2.22
Clash score	13.57	21.31	18.43	16.01
Ramachandran plot (%)				
Outliers	0.1	0.26	0.4	0.15
Allowed	3.67	7.33	9.49	4.18
Favored	96.24	92.42	90.12	95.67
Rama-Z (Ramachandran plot Z-score, RMSD)				
whole (N = 1036)	0.51 (0.26)	-2.23 (0.27)	-1.91 (0.29)	-0.18 (0.23)
helix (N = 214)	0.63 (0.34)	-1.96 (0.42)	-1.14 (0.41)	1.17 (0.31)
sheet (N = 286)	1.85 (0.32)	-0.40 (0.37)	0.54 (0.37)	0.86 (0.25)
loop (N = 536)	-0.64 (0.26)	-1.87 (0.26)	-2.35 (0.28)	-1.39 (0.23)
Rotamer outliers (%)	0.56	3.91	2.99	1.92
Peptide plane (%)				
Cis proline/general	11.6/0.2	6.2/0.0	3.3/0.0	8.6/0.1
Twisted proline/general	0.0/0.1	0.0/0.0	0.0/0.3	0.0/0.2
CaBLAM outliers (%)	3.04	5.63	7.32	3.45
ADP (B-factors)				
Iso/Aniso (#)	8440/0	6402/0	6242/0	10620/0
min/max/mean				
Protein	78.97/260.88/146.95	46.79/362.28/143.66	51.96/387.42/144.45	30.00/252.96/136.11
Nucleotide	---	---	---	---

Ligand	92.44/292.30/180.12	78.92/388.12/221.92	124.98/195.38/160.46	104.78/245.72/168.92
Water	---	---	---	---
Occupancy				
Mean	1	1	1	1
occ = 1 (%)	100	100	100	100
0 < occ < 1 (%)	0	0	0	0
occ > 1 (%)	0	0	0	0
Data				
Box: Lengths (Å)	(88.56, 101.52, 138.24)	(95.04, 87.48, 110.16)	(92.88, 92.88, 101.52)	(89.64, 128.52, 168.48)
Supplied Resolution (Å)	3.3	3.3	3.1	3.5
Resolution Estimates (Å), Masked				
d FSC (half maps; 0.143)	3.4	3.2	3.1	3.5
d 99 (full/half1/half2)	4.3/3.3/3.3	4.5/3.7/3.7	4.2/3.4/3.4	4.2/2.4/2.4
d model	3.7	3.3	3.1	3.9
d FSC model (0/0.143/0.5)	3.2/3.3/3.8	3.2/3.4/7.4	3.1/3.3/7.2	3.4/3.4/3.8
Resolution Estimates (Å), Unmasked				
d FSC (half maps; 0.143)	3.5	3.3	3.1	3.6
d 99 (full/half1/half2)	4.3/2.5/2.5	4.5/3.5/3.4	4.2/3.2/3.2	4.2/2.3/2.3
d model	3.8	3.3	3.1	3.9
d FSC model (0/0.143/0.5)	3.3/3.4/3.8	3.2/3.5/7.6	3.1/3.4/7.3	3.4/3.5/4.0
Map min/max/mean	-0.60/1.36/0.06	-0.65/1.68/0.09	-0.67/1.77/0.10	-0.82/1.83/0.05
Model vs. Data				
CC (mask)	0.82	0.57	0.59	0.79
CC (box)	0.81	0.65	0.68	0.74
CC (peaks)	0.70	0.41	0.48	0.60
CC (volume)	0.82	0.58	0.59	0.78
Mean CC for ligands	0.72	0.56	0.58	0.78

935

936 **Extended Data Table 2: Disulfide-linked peptides identified by cross-linking mass**
937 **spectrometry.** Disulfide-linked peptides identified for each TCR genotype. Peptides with an
938 XLinkX score greater than 30 are shown, as no native peptides were observed below this
939 threshold. Color coding as follows: green, expected native disulfide; cyan, expected engineered
940 disulfide; red, non-native disulfide or contaminant; magenta, off-target disulfide involving the
941 engineered cysteines.
942

	XLINKX SCORE	SEQUENCE 1	CHAIN 1	CYS 1	SEQUENCE 2	CHAIN 2	CYS 2
TCRα(WT), TCRβ(WT)							
	120.57	V[C]LATGFYPDHVEL	B	163	[C]QVQFY	B	228
	106.91	LT[C]DAEAK	G	46	GMYQ[C]K	G	87
	95.96	Q[C]AQDMNHEY	B	42	F[C]ASSY	B	110
	90.84	T[C]PQYPGSEILW	E	49	VN[C]NTSITW	D	37
	73.16	FPSPESS[C]DVK	A	228	AD[C]GFTSESY	B	263
	70.28	SVPEGENLVLN[C]SFTDSAIY	A	42	L[C]AVRPLY	A	109
	69.67	SNKSDFA[C]ANAF	A	206	SV[C]LF	A	156
	58.32	T[C]PQYPGSEILW	E	49	[C]QVQFY	B	228
	53.59	VFVN[C]NTSITW	D	37	GIYR[C]NGTDIY	D	73
	40.68	NNSIIPEDTFFPSPESS[C]DVK	A	228	ATLV[C]L	B	163
	30.56	T[C]PQYPGSEILW	E	49	YV[C]YPR	E	98
TCRα(S104C-V182C), TCRβ(WT)							
	120.8	LT[C]DAEAK	G	46	GMYQ[C]K	G	87
	106.26	V[C]LATGFYPDHVEL	B	163	R[C]QVQFY	B	228
	104.38	Q[C]AQDMNHEY	B	42	F[C]ASSY	B	110
	92.7	GIYR[C]NGTDIYK	D	73	VFVN[C]NTSITW	D	37
	80.51	SVPEGENLVLN[C]SFTDSAIY	A	42	L[C]AVRPLY	A	109
	78.49	SNKSDFA[C]ANAF	A	206	SV[C]LF	A	156
	72.7	T[C]PQYPGSEILW	E	49	[C]QVQFY	B	228
	72.62	IAASQPGD[C]ATY	A	104	ITDKT[C]LDMR	A	182
	70.28	SVPEGENLVLN[C]SFTDSAIY	A	42	[C]NGTDIY	D	73
	65.27	V[C]LATGFYPDHVEL	B	163	T[C]PQYPGSEILW	E	49
	60.55	SDFA[C]ANAF	A	206	ITDKT[C]L	A	182
	56.37	FPSPESS[C]DVK	A	228	AD[C]GFTSESY	B	263
	49.26	ITDKT[C]L	A	182	SV[C]LF	A	156
	48.23	T[C]PQYPGSEILW	E	49	VN[C]NTSITW	D	37
	45.66	T[C]PQYPGSEILW	E	49	YV[C]YPR	E	98
TCRα(WT), TCRβ(T130C-H172C)							
	99.32	QEDGSVLLT[C]DAEAK	G	46	GMYQ[C]KGSQNK	G	87
	96.82	Q[C]AQDMNHEY	B	42	F[C]ASSY	B	110
	88.95	FGEGSRL[C]VLEDLK	B	130	ATGFYPD[C]VELSW	B	172
	79.2	SNKSDFA[C]ANAF	A	206	SV[C]LF	A	156
	72.18	SVPEGENLVLN[C]SFTDSAIY	A	42	L[C]AVRPLY	A	109
	71.14	GIYR[C]NGTDIYK	D	73	VFVN[C]NTSITW	D	37
	63.42	L[C]VLEDLK	B	130	LT[C]DAEAK	G	46
	62.17	L[C]VLEDLK	B	130	SV[C]LF	A	156
	54.2	L[C]VLEDLK	B	130	F[C]ASSY	B	110
	53.77	T[C]PQYPGSEILW	E	49	L[C]VLEDLK	B	130

	53.5	FPSPESS[C]DVK	A	228	AD[C]GFTSESY	B	263
	47.92	T[C]PQYPGSEILW	E	49	[C]QVQFY	B	228
	41.91	L[C]VLEDLK	B	130	[C]QVQFY	B	228
	41.51	AD[C]GFTSESY	B	263	L[C]VLEDLK	B	130
	38.79	T[C]PQYPGSEILW	E	49	YV[C]YPR	E	98
	36.32	ATGFYPD[C]VEL	B	172	[C]LSSR	B	207
	34.92	VFVN[C]NTSITW	D	37	GMYQ[C]K	G	87
	30.54	LT[C]DAEAK	G	46	[C]QVQFY	B	228
TCRα(WT), TCRβ(K33C-L135C)							
	96.43	GIYR[C]NGTDIYK	D	73	VFVN[C]NTSITW	D	37
	95.43	LT[C]DAEAK	G	46	GMYQ[C]K	G	87
	90.79	ATLV[C]LATGFYPDHVEL	B	163	R[C]QVQFY	B	228
	81.71	LTVLED[C]K	B	135	ATLV[C]L	B	163
	81.57	Q[C]AQDMNHEY	B	42	F[C]ASSY	B	110
	81.57	LTVLED[C]K	B	135	[C]QVQFY	B	228
	79.2	SNKSDFA[C]ANAF	A	206	SV[C]LF	A	156
	76.07	T[C]PQYPGSEILW	E	49	[C]QVQFY	B	228
	72.9	SVPEGENLVLN[C]SFTDSAIY	A	42	L[C]AVRPLY	A	109
	69.49	LTVLED[C]K	B	135	F[C]ASSY	B	110
	65.27	V[C]LATGFYPDHVEL	B	163	T[C]PQYPGSEILW	E	49
	64.22	ATLV[C]LATGFYPDHVEL	B	163	ATLV[C]LATGFYPDHVEL	B	163
	53.91	T[C]PQYPGSEILW	E	49	VN[C]NTSITW	D	37
	48.05	V[C]LATGFYPDHVEL	B	163	SDFA[C]ANAF	A	206
	47.05	LTVLED[C]K	B	135	SV[C]LF	A	156
	45.66	V[C]LATGFYPDHVEL	B	163	SV[C]LF	A	156
	43.9	T[C]PQYPGSEILW	E	49	V[C]YPR	E	98
	36.08	FPSPESS[C]DVK	A	228	AD[C]GFTSESY	B	263
	35.13	T[C]PQYPGSEILW	E	49	LTVLED[C]K	B	135
	35.04	T[C]PQYPGSEILW	E	49	[C]AVRPL	A	109
	34.06	V[C]LATGFYPDHVEL	B	163	VLN[C]SFTDSAIY	A	42
	30.82	SDFA[C]ANAF	A	206	LTVLED[C]K	B	135

943